

INVITED REVIEW

This section of *Journal of Materials Research* is reserved for papers that are reviews of literature in a given area.

Texture-engineered ceramics—Property enhancements through crystallographic tailoring

Gary L. Messing,^{a),b)} Stephen Poterala, Yunfei Chang, Tobias Frueh, Elizabeth R. Kupp, Beecher H. Watson III, Rebecca L. Walton, and Michael J. Brova
Department of Materials Science and Engineering, The Pennsylvania State University, University Park, Pennsylvania 16802, USA

Anna-Katharina Hofer and Raul Bermejo
Institut für Struktur- und Funktionskeramik, Montanuniversität Leoben, Leoben 8700, Austria

Richard J. Meyer Jr.
Applied Research Laboratory, The Pennsylvania State University, University Park, Pennsylvania 16802, USA

(Received 31 January 2017; accepted 10 May 2017)

Texture-engineered ceramics enable access to a vast array of novel texture-property relations leading to property values ranging between those of single crystals and isotropic bulk ceramics. Recently developed templated grain growth and magnetic alignment texturing methods yield high quality crystallographic texture, and thus significant advances in achievable texture-engineered properties in magnetic, piezoelectric, electronic, optical, thermoelectric, and structural ceramics. In this paper, we outline the fundamental basis for these texture-engineered properties and review recent contributions to the field of texture-engineered ceramics with an update on the properties of textured lead-free and lead-based piezoelectrics. We propose that further property improvements can be realized through development of processes that improve crystallographic alignment of the grain structure, create biaxial texture, and explore a wider array of crystallographic orientations. There is a critical need to model the physics of texture-engineered ceramics, and more comprehensively characterize texture, thus enabling testing of texture orientation-property relations and materials performance. We believe that *in situ* measurements of texture evolution can lead to a more fundamental and comprehensive understanding of the mechanisms of texture development.

I. INTRODUCTION

The properties of ceramics are governed by a combination of intrinsic crystallographic and extrinsic microstructural characteristics. Many applications require the directional properties of single crystals, whereas others require the averaged isotropic properties of polycrystalline ceramics. Crystallographic texture is widely used to enhance the performance of anisotropic polycrystalline materials, especially when the use of single crystals is impractical or impossible. Single crystals are limited in most applications because they lack the mechanical integrity of polycrystalline ceramics and are often expensive, time-consuming to produce, and limited in size,

geometry, and compositional range. In contrast polycrystalline ceramics are mechanically robust, can be produced over an extensive range of compositions, and functional properties can be tailored more readily with a range of dopants. Textured polycrystalline ceramics possess directional, single crystal-like properties as well as mechanical reliability and compositional versatility.

In this review, the term texture describes the preferred crystallographic orientation of grains in a polycrystalline material. Our objective is to demonstrate how a variety of directional ceramic properties can be accessed with control of crystallography in bulk polycrystalline ceramics. Morphological texture seen in thermal barrier coatings or patterned grinding surfaces is not addressed in this review. While thin film processes yield extraordinary orientation control, this paper focuses on the opportunities and challenges associated with textured bulk ceramics.

Crystallographic texture enables access to a wide variety of anisotropic ceramic properties. As reviewed below, texturing has been used extensively to tailor the performance of magnetic, ferroelectric, thermoelectric,

Contributing Editor: Nahum Trivitzky

^{a)}Address all correspondence to this author.
 e-mail: messing@ems.psu.edu

^{b)}This author was Editor in Chief during the review and decision stage. For the *JMR* policy on review and publication of manuscripts authored by editors, please refer to <http://www.mrs.org/editor-manuscripts/>.

DOI: 10.1557/jmr.2017.207

and superconducting ceramics.^{1–4} For example, electrical properties can be enhanced by the elimination of high angle grain boundaries in materials with directional electronic or ionic conduction. Likewise, mechanical compliance and related properties, such as piezoelectricity, can be improved by limiting mechanical clamping caused by the misalignment of neighboring grains.² Continuity of properties across grain boundaries is the primary goal of crystallographic texture in noncubic optical ceramics because the alignment of optic axes of each grain eliminates Mie scattering of photons at grain boundaries.⁵ Fracture toughness of ceramic materials is often enhanced in layered or fibrous microstructures obtained by crystallographic texture.⁶ Alternately, crystallographic texture can be used to create microstructural anisotropy, such as columnar or tabular grains. Such anisotropic microstructures are useful for controlling electrical conductivity or dielectric properties in ceramics, since these properties strongly depend on grain boundary effects.⁷

Although texture describes any nonrandom grain alignment in a polycrystalline material, only specific symmetry patterns, such as fiber or sheet (biaxial) texture symmetries, result in enhanced or single crystal-like properties.² In fiber texture, a single crystallographic direction in each grain is preferentially aligned along a global texture axis, but grains are oriented randomly perpendicular to that axis. In sheet texture, grains are preferentially aligned in all three axes. These texture symmetries are illustrated in Fig. 1 with associated stereographic projections. In most textured materials, the property of interest is maximized along a single crystallographic direction, and fiber texture is sufficient to obtain enhanced single crystal-like properties. Sheet texture is substantially more difficult to produce as it requires simultaneous or sequential alignment of two crystallographic directions.

Crystallographic texture in ceramics is generally more difficult to produce than in metallic systems, where texture can be induced, or modified, via plastic

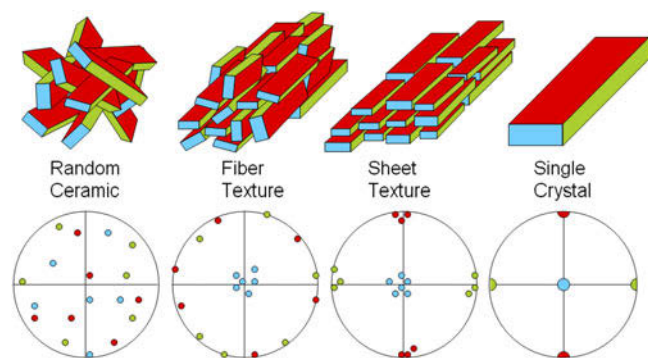


FIG. 1. Schematic illustrations and stereographic projections of fiber and sheet textures in a hypothetical biaxial (e.g., orthorhombic) ceramic.

deformation at lower temperatures than required for sintering and grain growth of ceramics. Some ceramics can be textured using high-temperature forging methods, but the temperatures required (e.g., 1750–1950 °C in Al_2O_3) make these methods impractical.^{8,9} During most ceramic fabrication processes, particles with aspect ratios other than unity are physically aligned. This incidental alignment persists during sintering and is often observed in ceramics fabricated by uniaxial pressing processes like die pressing, hot pressing, and spark plasma sintering. Subsequent sintering and grain growth lead to low quality (e.g., <20% texture fraction) crystallographic texture in these cases. Texture-engineered ceramics discussed in this paper are purposely textured by aligning crystalline powders before the sintering process and thus lead to texture fractions >90% in most cases.

The first widely studied texture-engineered ceramics were the magnetic hexaferrites, $\text{MeO} \cdot 6\text{Fe}_2\text{O}_3$ (Me = Ba, Sr) developed in the 1950s.¹ In the decade preceding this development, $\text{BaFe}_{12}\text{O}_{19}$ single crystals were shown to have ideal magnetic properties along [001] (the *c*-axis), making these materials interesting as permanent magnets. In comparison, hexaferrite ceramics showed poor performance relative to single crystals since only a small fraction of grains were *c*-axis oriented.¹⁰ In 1952, Rathenau et al. produced textured $\text{BaFe}_{12}\text{O}_{19}$ ceramics by applying a magnetic field along the pressing axis during the powder compaction process to develop a strong [001] orientation parallel to the direction of the applied field as a result of magnetic alignment (MA) of the plate-like $\text{BaFe}_{12}\text{O}_{19}$ particles.¹ This texture resulted in single crystal-like magnetic properties along the pressing direction. Because of the ease of the magnetic alignment process, [001] textured hexaferrite ceramics became the first widely studied and commercialized texture-engineered ceramic materials.

A large number of powder or sol-gel processing techniques are available for producing texture in ceramics. These processing methods are categorized by mechanical, electromagnetic, or thermal driving forces for particle alignment (Fig. 2). While all of these methods result in texture, it is noted that temperature is a scalar and cannot break symmetry (unlike mechanical and electromagnetic forces, which are vectors). As a result, uniformly applied heating alone cannot create texture, but enhances pre-existing textures via preferential growth of aligned grains. In contrast, thermal gradients may create primary texture, as seen in directional solidification.

Four general techniques have been developed in the last few decades to achieve ceramics with a high texture fraction (e.g., >90% of the material volume is textured), including the Rolling Assisted Biaxially Textured Substrates process (RABiTS, Fig. 3),¹¹ powder-in-tube (PIT),¹² templated grain growth (TGG) and reaction templated grain growth (RTGG),^{13,14} and strong (7–14 T) magnetic

field alignment (MA) of particles.¹⁵ The RABiTS process is shown in Fig. 3 and is included here because it leads to biaxial texture, which is an important objective for texture-engineered bulk ceramics.

The TGG process for producing crystallographically textured ceramics was first reported in 1997.¹⁶ This process develops crystallographic texture by first orienting a minority (e.g., 5 vol%) of micrometer scale anisotropic particles (e.g., platelets or whiskers) in a dispersion of submicrometer equiaxed particles. As seen in Fig. 2, anisotropic particles can be oriented by a number of methods. Most commonly, fiber texture is produced by aligning plate-like particles via tape casting a high viscosity dispersion under the shear field of a doctor

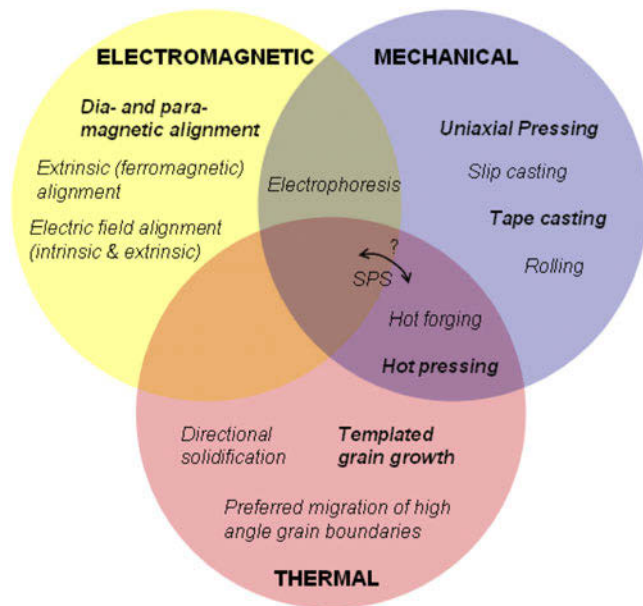


FIG. 2. Electromagnetic, mechanical and thermal processing methods utilized to produce grain alignment in ceramic materials. Most commonly used processing methods are shown in bold.

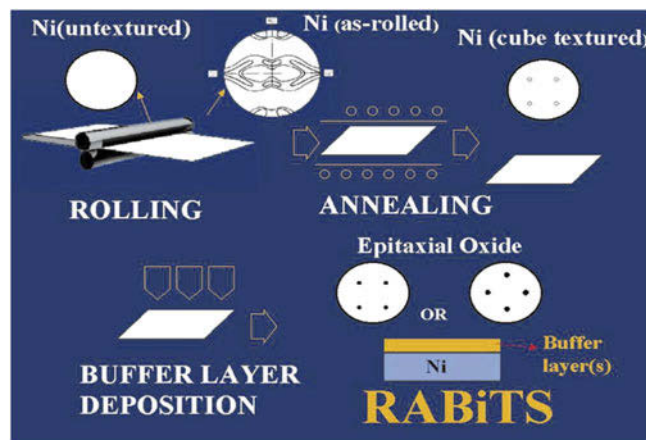


FIG. 3. Schematic of the RABiTS process. Reproduced with permission from Ref. 11.

blade. During subsequent sintering and heat treatment, the larger oriented particles serve as templates for epitaxial nucleation of similarly oriented grains, which grow via an Ostwald ripening process after densification (Fig. 4). The texture produced by TGG provides access to property anisotropy approaching that of the corresponding single crystal while also possessing the mechanical robustness of polycrystalline ceramics. Variations of this process include alternative means for aligning the template particles, simultaneous alignment in multiple directions to produce sheet textures or the use of a precursor matrix powder that subsequently crystallizes to the desired phase by reactive RTGG. The template particles can be identical in crystal structure to the host (homoepitaxial) or may differ substantially in lattice parameter or space group (heteroepitaxial). As shown in Fig. 4 the template may also form *in situ* by topochemical conversion.¹³ Since TGG-type processes utilize standard ceramic powder processing techniques, textured ceramics are potentially less expensive to produce than single crystals.

Sakka’s group was the first to show that textured ceramics can be produced by orienting weakly magnetic (diamagnetic or paramagnetic) particles in a suspension using a strong magnetic field of 7–14 T.¹⁵ Subsequent sintering of the oriented particles results in a high texture fraction. Under MA, particles in a suspension experience an alignment torque based on the intrinsic magneto-crystalline anisotropy (MCA)¹⁷:

$$T = \frac{VB^2}{2\mu_0} \Delta\chi \sin 2\theta \quad , \quad (1)$$

where B is the applied field, V is the particle volume, μ_0 is the permeability of free space, and $\Delta\chi$ is the para- or

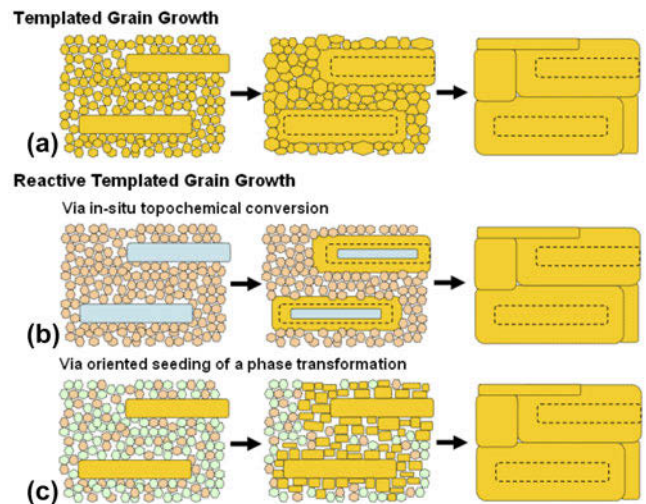


FIG. 4. Schematic of the TGG and reactive TGG process. The *in situ* topochemical conversion texturing process was first reported by Tani,¹³ whereas the oriented seeding of a phase transformation texturing process was developed by Yilmaz et al.¹⁴

diamagnetic anisotropy of the aligned material. The alignment torque is opposed by viscous resistance of the surrounding fluid. MA of particles is not dependent on particle morphology, and the factors controlling alignment (field strength, particle size, viscosity) are easier to experimentally control than particle aspect ratio. As with all colloidal dispersions, steady state alignment in MA systems is opposed by the randomizing effect of Brownian motion.

II. TEXTURE MEASUREMENTS

Developing fundamental relations between crystallographic orientation and properties requires measurements to determine not only the texture fraction but also the quality of grain alignment. Texture analysis is most commonly conducted by X-ray diffraction, but electron and neutron diffraction may also be used depending on the type of sample being analyzed. Electron and X-ray diffraction have less bulk penetrating capabilities than neutrons, so for materials that impede X-rays (e.g., lead-containing ceramics), neutron diffraction is an attractive choice.¹⁸ Scans of 2θ by these methods can be analyzed using the intensities of specific peak heights of interest normalized to those of the untextured sample. This method is widely favored and results in the Lotgering factor (LF or $f_{(00l)}$).¹⁹ For example, the LF of the $00l$ orientation is:

$$f_{(00l)} = \frac{P_{(00l)} - P_0}{1 - P_0} \quad (2)$$

$$P_{(00l)} = \frac{\sum I_{(00l)}}{\sum I_{(hkl)}} \text{ and } P_0 = \frac{\sum I_{0(00l)}}{\sum I_{0(hkl)}} ,$$

where $\sum I_{(00l)}$ is the summation of the peak intensities of all $00l$ peaks (i.e., 001, 002, . . .) in the textured sample pattern. $\sum I_{(hkl)}$ is the summation of the peak intensities of all hkl peaks which appear in the XRD pattern. $\sum I_{0(00l)}$ and $\sum I_{0(hkl)}$ are summations of the XRD peak intensities for an untextured sample. The Lotgering factor scales between 0 and 1 and the value is often expressed as a percentage.

It should be noted that while the Lotgering factor is a measure of the oriented material, it does not accurately account for how well the grains are aligned.¹⁹ Unfortunately, due to the ease of measurement and calculation, the LF is most often the only measure of texture reported. For some of the properties discussed below, it is apparent that more quantitative and comprehensive texture measures are necessary to provide fundamental insights into how texture fraction and grain alignment affect properties.

Similar analysis of the 2θ scans from X-ray or neutron diffraction was conducted by Jones et al.,¹⁸ which uses the integrated intensity of the peaks, thereby producing more quantitative comparisons between samples. The method for texture analysis of a material with both tetragonal and orthorhombic phases is shown in Eq. (3), where I_{00h}^R is the

integrated intensity for a randomly oriented sample and I_{00h} and I_{h00} are from the textured sample.

$$\text{Tetragonal : } f_{001}(\text{mrd}) = 3 \frac{I_{00h}/I_{00h}^R}{I_{00h}/I_{00h}^R + 2I_{h00}/I_{h00}^R}$$

$$\text{Orthorhombic : } f_{100}(\text{mrd}) = 2 \frac{I_{h00}/I_{h00}^R}{I_{h00}/I_{h00}^R + 2I_{0h0}/I_{0h0}^R} \quad (3)$$

The orientation distribution function (ODF) of the grains, which represents the probability of a given crystal orientation relative to a randomly oriented material,¹⁸ can be measured by rocking curves and pole figures which are obtained by X-ray, electron, or neutron diffraction. The ODF of the individual grain orientation can be evaluated by stereology on micrographs when the grain shape is anisotropic, or the data can be automatically obtained from electron backscatter diffraction (EBSD). Brosnan et al. showed that while XRD rocking curve, XRD pole figure, and EBSD data yielded similar f , r , and FWHM values for [001] textured PMN–PT, the XRD rocking curve analysis was the most efficient method and gave a more complete description of texture fraction and texture orientation since it sampled a larger fraction of the material during analysis.²⁰ The data generated by these analysis methods is shown in Fig. 5.

The March–Dollase equation was developed to quantify both texture fraction and quality of orientation. In this equation, the ODF $[F(f, r, \omega)]$ is given by:

$$F(f, r, \omega) = f \left(r^2 \cos^2 \omega + \frac{\sin^2 \omega}{r} \right)^{-\frac{3}{2}} + (1 - f) \quad (4)$$

where ω is the angle between the texture (orientation) axis and the scattering vector, f is the volume fraction of oriented material, r is the degree of orientation of the oriented material, and $(1 - f)$ is the volume fraction of randomly oriented material. Note that the f value obtained from the March–Dollase fit is not equal to the $f_{(00l)}$ calculated from the Lotgering factor equation. The r parameter characterizes the width of the texture (orientation) distribution. For an untextured sample $r = 1$ and for a perfectly aligned sample of tabular grains $r = 0$.²¹ The March–Dollase equation can be simplified to the multiples of random distribution (MRD) by assuming $f = 1$ (a completely textured sample), thus allowing for the texture equation to be a function of only two variables, r and ω . The form of the MRD is given by:

$$\text{MRD}(r, \omega) = \left(r^2 \cos^2 \omega + \frac{\sin^2 \omega}{r} \right)^{-\frac{3}{2}} \quad (5)$$

Equation (5) is graphed in Fig. 6 to illustrate the effect of r on the shape and FWHM of the March–Dollase fit.

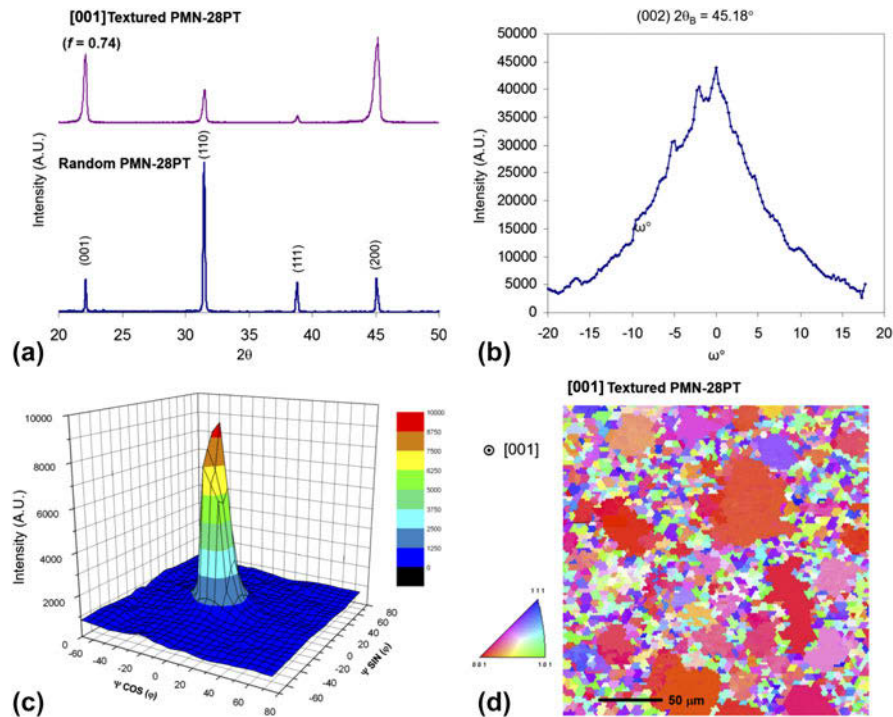


FIG. 5. Evaluation of texture by (a) X-ray diffraction analysis using the Lotgering factor, (b) full-width at half-maximum peak analysis, (c) pole figure analysis and (d) EBSD for [001] textured PMN-28PT. Reproduced with permission from Ref. 20.

III. TEXTURED MAGNETIC CERAMICS

The majority of commercially produced magnetic ceramics, or ferrites, contain chemical combinations of some magnetic species, typically iron. As previously discussed, the first commercial textured ceramics were [001] textured $\text{BaFe}_{12}\text{O}_{19}$. Magnetic properties exhibit a pronounced crystallographic directional dependence, or MCA. MCA in magnetic materials originates primarily from spin-orbit interaction of electrons. Since electron orbits are determined by crystal structure, different crystallographic directions, planes (ferroplana), or cones result in different propensities for electron alignment.²² In a practical sense, specific crystallographic directions are commonly referred to as “easy” axes because magnetization in these directions requires less energy, and the opposite is true for “hard” axes. Crystal systems often have easy planes and cones, which have a lower energy barrier for magnetization.²³

The majority of ferrite compounds are classified as cubic ferrites or hexagonal ferrites (hexaferrites).²³ Crystal systems with an axis of high symmetry exhibit uniaxial anisotropy, and the crystallographic easy axes switch at specific temperatures making temperature an important consideration when aligning magnetic materials. For instance, in the $\text{Ba}_3\text{Co}_2\text{Fe}_{24}\text{O}_{41}$ hexaferrite system, the preferred direction for magnetization above 207 °C is the *c*-axis. Below 207 °C, the basal plane (ferroplana) becomes the easy magnetization plane, and

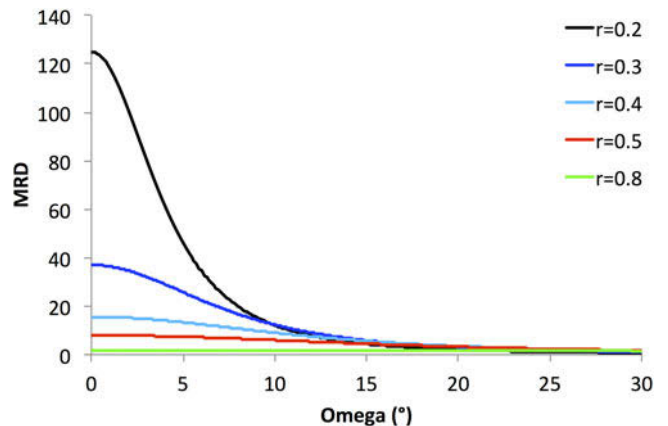


FIG. 6. MRD functions for different *r* values where each line represents a hypothetical March-Dollase fit for a particular quality of texture.

below -53 °C a cone encapsulating the *c*-axis is easier to magnetize.²⁴ It is also worth mentioning that lattice strain results in abnormal lattice parameters that affect the magnetization direction dependence slightly.²⁴

Within crystalline materials, electron alignment exists in coherent localized regions called domains that usually align with the easy axes. One grain may contain multiple domains or one domain may contain multiple grains, depending on grain and domain sizes.²³ Domains align under an applied magnetic field, and the amount of energy required is called the coercivity or H_c .²³ The

coercivity value is largely determined by crystallographic defects such as grain boundary misorientation, dislocations, or impurities which can pin domain movement. Furthermore, total material magnetization (when all the domains are aligned) is referred to as magnetic saturation M_s . After the external field is removed, the domains reorient themselves with the easy axes, and the residual magnetization is called remanence or M_r .²³

In a ferrite, the degree of crystallographic orientation, with respect to the easy and hard axes, corresponds greatly to the magnetic remanence and slightly to the magnetic coercivity. Typically, M_r approaches M_s as texture quality improves, and the coercivity decreases slightly with increasing orientation as the grain boundary coherency improves. Greater coherency weakens the domain wall pinning mechanism.²³

The effect of crystallographic alignment on magnetic properties was first observed for a textured $\text{BaFe}_{12}\text{O}_{19}$ M-type hexaferrite fabricated by magnetic alignment of a high solids content slurry of $\text{BaFe}_{12}\text{O}_{19}$ particles within an 11,000 Oe magnetic field. Textured $\text{BaFe}_{12}\text{O}_{19}$ ceramic had a magnetic remanence of 0.37 T and coercivity of 1200 Oe parallel to the basal plane while untextured $\text{BaFe}_{12}\text{O}_{19}$ had a magnetic remanence of 0.205 T and coercivity of 2600 Oe. Additionally, the magnetic properties were measured in different crystallographic directions (Fig. 7). While the texture fraction and degree of crystal orientation were not mentioned, this study effectively showed an avenue by which magnetic properties could be tailored using crystallographic orientation.

There is surprisingly little literature about textured bulk magnetic ceramics since the Rathenau study. In recent years, the advent of techniques for substantially improved texture quality such as TGG and RTGG, and high magnetic field alignment has renewed interest in oriented ferrites. In 2011, Chen et al. uniaxially pressed $\text{Ba}_3\text{Co}_2\text{Fe}_{24}\text{O}_{41}$ Z-type ferrites in a rotating in-plane magnetic field²⁵ and sintered them for 2–16 h in air at 1200–1280 °C. This process resulted in Lotgering factors ($f_{(001)}$) of 0.3–0.5 with high magnetic remanence and low coercivity relative to untextured $\text{Ba}_3\text{Co}_2\text{Fe}_{24}\text{O}_{41}$.²⁵ In 2014, Jian et al. aligned needle-shaped $\alpha\text{-FeOOH}$ template particles in CoO and Fe_2O_3 powders to produce [001] textured CoFe_2O_4 ferrites with $f_{(001)}$ of 0.81 by RTGG.²⁶ Magnetic properties of untextured and textured CoFe_2O_4 samples are compared in Fig. 8. The textured ceramic had higher saturation and remnant magnetization of 355 emu/cm^3 and 90 emu/cm^3 in plane, respectively, and 260 emu/cm^3 and 15 emu/cm^3 out of plane, respectively. By comparison, the untextured ceramic had an M_s of 320 emu/cm^3 and M_r of 87 emu/cm^3 .²⁶ Chang et al. used RTGG to create textured $\text{Ba}_3\text{Co}_2\text{Fe}_{24}\text{O}_{41}$ by tape casting $\text{BaFe}_{12}\text{O}_{19}$ platelets in a $\text{Ba}_2\text{Co}_2\text{Fe}_{12}\text{O}_{22}$ hexaferrite powder matrix.²⁷ While the $f_{(001)}$ was only 0.39, the textured ceramic had increased magnetic permeability

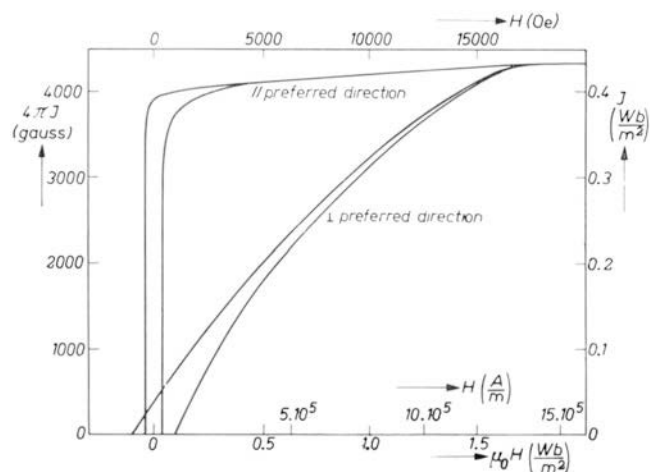


FIG. 7. Hysteresis loops (upper half only) of an isotropic Ferroxdure sample sintered at a high temperature measured parallel and perpendicular to the preferred direction (c -axis). The magnetic texture closely resembles that of a single crystal. Reproduced with permission from Ref. 24.

relative to the untextured sample, and reduced coercivity was observed perpendicular to the c -axis.²⁷

IV. TEXTURED SUPERCONDUCTORS

Superconductors are a unique class of materials that display zero resistance to the flow of electricity below a critical temperature (T_c),²⁸ making these materials attractive choices for advanced electrical conductors and powerful magnets. In 1986, high temperature superconducting (HTS) cuprate-based ceramics, including $\text{YBa}_2\text{Cu}_3\text{O}_{7-\delta}$ (YBCO), were discovered to exhibit superconducting properties below 93 K. The development of materials with T_c higher than the boiling temperature of N_2 (77 K) was a significant achievement because it resulted in easier and less expensive cooling for superconductivity. A variety of other HTS materials have been discovered, such as the Bi–Sr–Ca–Cu–O (BSCCO) family.²⁹

In power transmission lines, YBCO-coated tapes and power cables with very high critical current density, J_c , of 10^6 – 10^7 A/cm^2 in zero-field were fabricated using the RABiTS process.^{30,31} The RABiTS process was developed by Goyal et al.³² to produce biaxially textured superconducting wires and tapes. The RABiTS process achieves biaxial or sheet texture by taking advantage of the biaxial texture produced in rolled cubic metals and FCC and BCC alloys after recrystallization. Ni and Ni–W–Cr alloys are the most commonly used metals for the RABiTS process. The texture of the crystallized metal strip (e.g., 1 cm wide by 10 m in length) consists of a {100} cube plane parallel to the plane of the strip and a cube edge parallel to the rolling direction. Buffer layers, such as YSZ, are deposited on the metal strip by a number of thin film processes to mediate diffusion of the metal into the superconducting layer ($\sim 1 \text{ }\mu\text{m}$ thick).

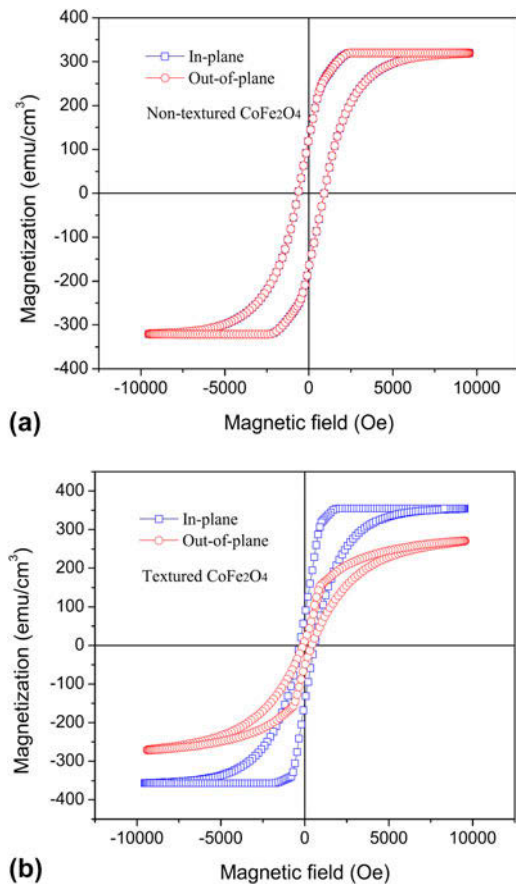


FIG. 8. Room temperature magnetic hysteresis loops of CoFe_2O_4 ceramics after sintering at 1150°C for 4 h: (a) untextured and (b) textured along the [001] direction. Reproduced with permission from Ref. 26.

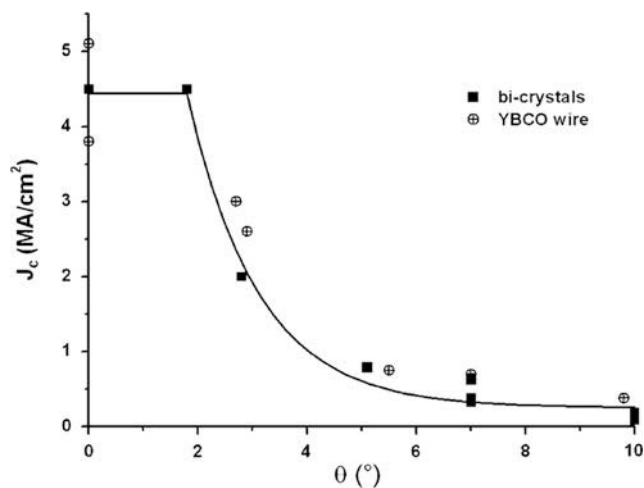


FIG. 9. The critical current density as a function of total grain boundary misorientation angle for both $\text{YBa}_2\text{Cu}_3\text{O}_{7-x}$ (YBCO) films deposited on SrTiO_3 bicrystal substrates and polycrystalline YBCO wires. The solid line is a fit to the bicrystal data. The data were taken at 77 K and self-field. Reproduced with permission from Ref. 31.

Additionally, the use of a buffer layer(s) minimizes both lattice mismatch and thermal expansion differences between the metal substrate and deposited superconducting layer. The process has not been applied to bulk ceramics.

The PIT process is another technique for fabrication of superconducting tapes and wires, primarily for ferropnictides and BSCCO materials. A silver tube is filled with superconductor powder and then the tube is cold worked, flat rolled, and groove rolled to produce wires of various thicknesses and diameters. The process controls crystallographic orientation at low temperature while maintaining very small grain sizes. Susner et al. fabricated superconducting PIT MgB_2 wires.³³ They reported no anisotropy in current density at zero field, but as the applied magnetic field (applied perpendicular to the wire axis) increased, they measured an increasing anisotropy. At 8 T, the critical current density parallel to the wire axis was $J_c \sim 10^4 \text{ A/cm}^2$, while perpendicular to the axis, $J_c \sim 10^3 \text{ A/cm}^2$. Texture was reported as a function of particle aspect ratio, but no quantitative texture analysis was performed.

The critical current density is highly dependent on grain to grain connectivity and alignment. It has been shown that critical current density decreases exponentially above $2\text{--}3^\circ$ of misorientation in the $a\text{--}b$ plane even with a high degree of [001] orientation (Fig. 9).³⁴ The strong dependence of J_c on the misorientation angle has led to research to minimize crystallographic misorientation, and to further improve current carrying capacities of HTS.

Untextured HTS ceramics have poor $J_c \sim 10\text{--}10^2 \text{ A/cm}^2$ as a result of weak-link coupling of misaligned polycrystalline grains.²⁹ Thus, bulk HTS production has been limited primarily to single crystal growth. However, the excellent properties of HTS single crystals is a strong motivation for research on fabrication of bulk textured HTS ceramics.^{35,36} The fabrication of bulk textured HTSs by slip casting,³⁷ tape casting,^{38,39} and extrusion⁴⁰ has been explored. The shear forces generated using these techniques contribute to grain alignment of anisotropic grains and J_c is improved to $\sim 10^3 \text{ A/cm}^2$. Using a sharp thermal gradient, geometric constraint of thin samples, or casting onto textured substrates, grain alignment has been increased to yield J_c of $\sim 10^4 \text{ A/cm}^2$.^{40,41}

V. TEXTURED ION CONDUCTORS

Ceramics with high rates of either anion or cation conduction form an important class of materials that are finding applications as ion conducting membranes in fuel cells, and as high temperature, e.g. Na-S, battery electrolytes. Beta alumina has a hexagonal crystal structure and refers to all types of β and β' aluminas incorporating Na^+ , K^+ , NH_4^+ , or H_3O^+ . The Na^+ ion can be exchanged for K^+ , NH_4^+ , or H_3O^+ . Na- β and Na- β' aluminas, stabilized by the addition of Mg^{2+} or Li^+ , are

two of the most extensively used cationic conductors in high temperature batteries. These materials consist of alumina spinel layers separated by 2-dimensional conduction planes. In the conduction planes oxygen ions form bridges between two adjacent alumina spinel layers and sodium ions sit in specific crystallographic positions in the conduction planes, known as Beevers–Ross sites. The ionic conduction in beta alumina occurs by the migration or hopping of sodium ions between Beevers–Ross sites and anti-Beevers–Ross sites.^{42–44} Beta alumina batteries must be operated at 300 °C to achieve sufficiently high ionic conductivity. Ionic conduction through beta alumina grains occurs only along the conduction planes perpendicular to the *c*-axis.

In polycrystalline beta alumina, current carrying ions travel across the grain boundaries from the conduction plane of one grain to the conduction plane of another grain. The ionic conductivity of the grain boundary depends on the misorientation angle between the grains, i.e., low misorientation angles between the crystal lattices of the adjacent grains have a lower resistance than high misorientation angles.^{7,45–48} The ionic conductivity of untextured polycrystalline beta alumina is 3–5 times lower than the ionic conductivity of a beta alumina single crystal measured parallel to the conduction plane.⁴⁹ The increased conductivity of textured beta alumina parallel to the conduction planes is attributed to reduced misorientation angles between grains,^{7,47,50,51} in addition to less tortuous and shorter conduction pathways.^{7,47,48,50}

Fabrication of textured beta aluminas with preferred crystallographic orientations using uniaxial dry pressing,^{48,50,52–54} hot pressing,^{7,48,55–57} spark plasma sintering,⁵⁸ microwave sintering,⁵⁹ and slip casting under a magnetic field has been reported.^{60,61} However, the number of systematic studies on how the degree of misorientation and quality of texture in beta aluminas affects the ionic conductivity is scant. Some authors report textured microstructures based on qualitative microscopy,^{54,55} while others compare relative X-ray diffraction peak heights,^{50,57,61} or report orientation or texture coefficients,^{7,59,60} Thus, it is difficult to evaluate and compare the quality and degree of texture of these materials.

Lotgering factors ($f_{(001)}$) of 0.30–0.43 were reported by Koganai et al.⁵⁸ and Asaoka et al.,⁵⁶ and Kishimoto⁴⁸ obtained $f_{(001)}$ values of up to 0.58 for oriented beta aluminas. Even with low texture qualities, they observed up to an order of magnitude higher ionic conductivities along the texture direction compared to the ionic conductivity perpendicular to the texture direction.⁵⁶ It would be worthwhile to investigate how much the ionic conductivity can be increased by improving texture quality of textured beta alumina, since increased ionic conductivity may improve the efficiency of beta alumina high temperature batteries and reduce operation temperatures.

Proton and anion conductors are of interest for solid oxide fuel cells, gas sensors, and gas separation membranes. Materials of interest for such applications include Aurivillius phases, perovskite- and Brownmillerite-like phases derived from $\text{Ba}_2\text{In}_2\text{O}_5$, and Si- and Ge-based apatite structures. $\text{Bi}_4\text{V}_2\text{O}_{11}$, for example, is an Aurivillius phase that consists of alternating $(\text{Bi}_2\text{O}_2)^{2+}$ and perovskite-like $(\text{VO}_{3.5})^{2-}$ layers with oxygen vacancies in the $\text{VO}_{3.5}^{2-}$ layers. Oxygen is conducted by a vacancy mechanism through the 2-dimensional oxygen deficient perovskite layers.^{62–64} $\text{Ba}_2\text{In}_2\text{O}_5$, and derivatives thereof, have been explored as oxygen and proton conductors.^{62,64,65} $\text{Ba}_2\text{In}_2\text{O}_5$ consists of alternating layers of corner sharing InO_6 octahedra and layers of InO_4 tetrahedra. The perovskite layers are oxygen deficient, and the vacancies are ordered along the [010] direction forming one-dimensional paths for oxygen ion or proton diffusion in the tetrahedral layers. In apatite structures such as $\text{La}_{9.33}(\text{SiO}_4)_6\text{O}_2$, isolated SiO_4 tetrahedra align to form channels parallel to the *c*-axis with a row of oxygen ions in the center.^{62,64–66} It is apparent that the discussed anion and proton conductors possess significant anisotropy in ionic conductivity and a substantial improvement in the ionic conductivity could be achieved by texturing, as indicated by the work of Fukuda et al.⁶⁷

VI. TEXTURED THERMOELECTRICS

Textured thermoelectric (TE) ceramics have recently emerged as an important application for texture-engineering. Thermoelectric devices require a combination of a high electrical conductivity and low thermal conductivity to maximize the thermoelectric conversion efficiency. The thermoelectric figure of merit is $ZT = S^2\sigma T/k$ where S is the Seebeck coefficient, σ the electrical conductivity and k is the thermal conductivity. Recent interest in ceramics for TEs has increased as researchers develop new means to recover lost heat from automobile exhaust and power plants. For the best thermoelectric materials today $ZT = 1$ and scientists are searching for ways to further increase ZT . The reader is directed to Medlin and Snyder's review of the processing and properties of conventional TEs like PbTe and Bi_2Te_3 .⁶⁸ There are many reports in this review about how to increase TE performance through crystallographic texture, reduction of grain size, and utilization of nanostructuring strategies. Interestingly, the texturing approaches used for ceramics have yet to be explored for these systems.

Oxide ceramics are of special interest since they are stable in air and can operate at elevated temperatures where conventional TEs oxidize. Ceramic TEs have been extensively studied since the late 90s when a variety of cobaltites were proposed as potentially good thermoelectrics.^{69–71} Hejtmanek et al. predicted that Na_xCoO_2

and $\text{Ca}_3\text{Co}_4\text{O}_9$ single crystals and thin films would have a $4\times$ lower electrical resistivity in the ab plane and thus these materials should have a theoretical ZT of 4.⁷² Tani developed the RTGG process to texture a variety of these layered structure materials since anisotropic electric conductivity is important for TE applications, similar to Bi_3Te_2 .¹³ He developed a process in which the template is consumed during the process and thus there is no relic of the template grains in the textured ceramic [see Fig. 4 (b)].⁷³ As an example, platelike $\beta\text{-Co(OH)}_2$ particles were aligned in a matrix powder of CaCO_3 . Upon heating the materials underwent phase changes until $[001]$ textured $[\text{Ca}_2\text{CoO}_3]_{0.62}[\text{CoO}_2]$ formed. The properties were anisotropic with the electrical conductivity being 60% of the single crystal value. He showed that the electrical conductivity was strongly dependent on the FWHM of the oriented grain structure and pointed out the importance of ‘ultimate’ texture for application of textured thermoelectric ceramics.¹³

More recently, Koumoto et al. reviewed the status of thermoelectric ceramics.⁷⁴ They compared the behavior of $\text{Ca}_3\text{Co}_4\text{O}_9$ ceramics textured by RTGG, magnetic alignment and SPS.^{75–82} Although well-oriented ceramics with high texture fraction were produced, the ZT values were lower than predicted for single crystals. They also showed that while the electrical conductivity and thermal conductivity of $[001]$ textured $\text{Ca}_3\text{Co}_4\text{O}_9$ are strongly orientation dependent, the Seebeck coefficient is nearly temperature independent and the same for the untextured, c -axis and ab -plane oriented samples.⁸³

Lee et al. recently reported that non-stoichiometric $\text{Sr}_x\text{Ba}_{1-x}\text{Nb}_2\text{O}_6$ single crystals are promising n-type thermoelectrics.⁸⁴ In a subsequent paper they textured SBN by RTGG using rod-shaped particles of $\text{Ba}_2\text{NaNb}_5\text{O}_{15}$.⁸⁵ The c -axis textured ceramic resulted in higher thermopower and electrical conductivity than the untextured ceramic. The above results show that TE applications of textured ceramics require both a high texture fraction and a narrow distribution of grain alignment due to the importance of electrical conductivity.

VII. TEXTURED PIEZOELECTRICS

Piezoelectricity describes the ability of non-centrosymmetric materials to develop an electric polarization proportional to an applied mechanical stress (direct piezoelectric effect), or to develop a mechanical strain (deformation) proportional to an applied electric field (converse piezoelectric effect). Piezoelectrics are essential components in a wide range of applications, including ultrasonic transducers, sensors, and actuators. The next generation of piezoelectric applications requires a significant increase in typical figure of merit coefficients (e.g., piezoelectric coefficient d_{ij} , electromechanical coupling coefficient k_{ij} and mechanical quality factor Q_m).

The large piezoelectric effect exhibited for domain-engineered single crystals represents a significant advance in piezoelectric materials. By controlling grain orientation, textured piezoelectric ceramics have emerged as an alternative to single crystals. In this case the textured piezoelectrics can be domain-engineered like single crystals but at the grain by grain level (Fig. 10).

The most commonly used piezoelectrics are perovskites (general formula ABO_3), tungsten-bronze structures, Aurivillius phases (or bismuth-layered structures), and perovskite layer structures. Tables I, II, SI and SII summarize the data since the 2004 review of textured piezoelectric ceramics² as a function of crystal class showing the piezoelectric coefficients of different types of textured ceramics as a function of template type and texture fraction.

A. Textured perovskite piezoelectrics

Lead-based ceramics such as Pb(Zr,Ti)O_3 (PZT), $\text{Pb(Mg}_{1/3}\text{Nb}_{2/3})\text{O}_3\text{-PbTiO}_3$ (PMN–PT), and $\text{Pb(In}_{1/2}\text{Nb}_{1/2})\text{O}_3\text{-Pb(Mg}_{1/3}\text{Nb}_{2/3})\text{O}_3\text{-PbTiO}_3$ (PIN–PMN–PT), as well as lead-free ceramics like $(\text{K,Na})\text{NbO}_3$ (KNN), $\text{Bi}_{1/2}\text{Na}_{1/2}\text{TiO}_3$ (BNT), and BaTiO_3 (BT) ceramics belong to the large family of perovskite ceramics. They are of greatest interest because of their exceptional piezoelectric properties.

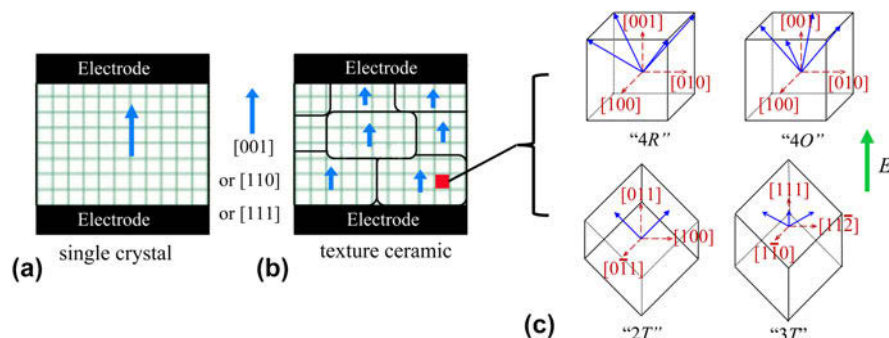


FIG. 10. Schematic diagram of (a) a single crystal piezoelectric device with $[001]$, $[110]$ or $[111]$ orientations, (b) a textured polycrystalline ceramic with the same orientation, and (c) some domain-engineered states such as “4R”, “4O”, “2T”, and “3T”.

TABLE I. Piezoelectric coefficients (d_{33}) of [001] textured lead-based ceramics and isotropic ceramics.

Composition	Template	Lotgering factor ($f_{(00l)}$)	Piezoelectric coefficient (pC/N)	Degree of enhancement
Pb(Zr,Ti)O ₃ ⁸⁶	...	0.77	$k_{31} = 0.44$	1.3×
PMN-32.5PT ⁸⁷	BT	0.90	$d_{33}^* = 1150$	1.6×
PMN-32PT ⁸⁸	BT	0.99	$d_{33}^* = 878$	1.8×
PMN-32.5PT ⁸⁹	BT	0.98	$d_{33}^* = 1000$	2×
PMN-28PT ⁹⁰	ST	0.86	$d_{33} = 940$	0.64×
				(single crystal)
PMN-32.5PT ⁹¹	PMN-PT	0.78	$d_{33}^* = 1000$...
PMN-28PT ⁹²	NBT-PT	0.92	$d_{33} = 1016$	3.4×
[111]-PMN-40PT ⁹³	[111]-BT**	0.95	$d_{33} = 270$	1.3×
PT ⁹⁴	NBT-PT	0.95	$d_{33} = 127$	2.4×
PIN-PMN-32PT ⁹⁵	BT	0.93	$d_{33} = 820$	2×
PIN-PMN-34PT ⁹⁶	BT	0.95	$d_{33} = 780$	2×
PYN-PMN-38PT ⁹⁷	BT	0.91	$d_{33}^* = 1340$	1.6×
PMN-PZT ⁹⁸	BT	0.90	$d_{33} = 1100$	4.8×
[111]-PMN-PZT ⁹⁹	[111]-BT**	0.72	$d_{15} = 940$	2.6×

d_{33}^* calculated from the slope of the decreasing field on the strain-electric field curve.

**We replaced $\langle hkl \rangle$ with $[hkl]$ because it more accurately represents the measured property.

B. Lead-based piezoelectrics

Lead-based piezoelectrics have dominated the piezoelectric market since 1950s due to the high dielectric and piezoelectric properties achieved with compositions close to the morphotropic phase boundary (MPB). Highly [001]_c oriented compositionally modified Pb(Zr,Ti)O₃ (PZT) ceramics were successfully fabricated by slip casting in a high magnetic field.⁸⁶ A high k_{31} value of 0.44 (1.3 times higher than that of its untextured oriented counterpart) was achieved in the [001]_c oriented ceramics with a Lotgering factor ($f_{(001)}$) of 0.77.

Textured relaxor ferroelectric Pb(Mg_{1/3}Nb_{2/3})O₃-PbTiO₃ (PMN-PT) ceramics have attracted attention due to the much higher piezoelectric properties than PZT-based ceramics. BaTiO₃ (BT),⁸⁷⁻⁸⁹ SrTiO₃ (ST),⁹⁰ PMN-PT,⁹¹ and (Na_{1/2}Bi_{1/2})TiO₃-PbTiO₃ (NBT-PT)⁹² templates have been used to texture [001]_c oriented rhombohedral PMN-PT ceramics with compositions near the MPB by TGG. Ninety percent textured PMN-PT ceramics were initially produced by Sabolsky et al. using coarse (75–150 μm) tabular BaTiO₃ templates.⁸⁷ The measured d_{33}^* and T_c values were 1150 pC/N and 164 °C, respectively, but the resulting large grain sizes reduced the mechanical properties of the textured ceramics.

Subsequent work on textured PMN-PT ceramics focused largely on developing smaller templates with

TABLE II. Piezoelectric coefficients (d_{33}) of [001] textured lead-free ceramics and isotropic ceramics.

Composition	Template	Lotgering factor ($f_{(00l)}$)	Piezoelectric coefficient (pC/N)	Degree of enhancement
KNLNTS ¹⁰¹	NN	0.91	$d_{33} = 416$	1.6×
KNNS ¹⁰⁶	NN	0.97	$d_{33} = 208$	1.4×
KNLN ¹⁰⁷	NN	0.98	$d_{33} = 192$	1.7×
KNN ¹⁰⁹	NN	0.80	$d_{33} = 390$	1.2×
1% CuO-KNN ¹⁰⁸	NN	0.96	$d_{33} = 123$	1.4×
1% CuO-KNN ¹¹⁰	KN	0.40	$d_{33} = 68$	Slightly decreased
KNN ¹¹¹	KNN	0.86	$d_{33}^* = 282$	1.5×
0.5%CuO-KNN ¹¹²	NN	0.93	$d_{33} = 133$	1.3×
NBT-ST115	ST	0.82	$d_{33}^* = 557$	1.4×
NBT-KBT-BT ¹¹⁶	B4TO	0.60	$d_{33} = 254$	1.4×
BNT-BKT ¹¹⁷	B4TO	0.61	$d_{33} = 134$...
BNT ¹¹⁸	HTO	0.95	$d_{33}^* = 100$	1.4×
BNT-BKT ¹¹⁹	NN	0.91	$d_{33} = 217$	1.4×
BNT-BKT ¹²⁰	Al ₂ O ₃	0.70
BNT-BT ¹²³	BNT	0.92	$d_{33} = 322$	2×
KBT-BT-NBT ¹²⁴	BNT	0.93	$d_{33} = 192$	1.7×
BNT-BT-AN ¹²⁵	BNT	0.71	$d_{33}^* = 766$	1.8×
BNT-BT-KNN ¹²⁶	BNT	0.83	$S = 0.226\%$	1.5×
BT ¹²⁷	BT	0.97	$d_{33} = 274$	1.5×
[110]-BT ¹²⁹	[110]-BT**	0.85	$d_{33} = 788$...
[111]-BT ¹³⁰	[001]-NN**	0.95
[111]-BT131	[111]-BT**	0.66
BCZT133	BT	0.82	$d_{33} = 470$	1.3×
BZT134	ST	>0.90	$d_{33}^* = 975$	3.2×
BCZT135	BT	0.70	$d_{33} = 462$	1.1×
BCT138	BT	0.96	$d_{33} = 207$	1.4×
BCT137	BT + CT	0.83	$d_{33} = 170$	1.2×

d_{33}^* calculated from the slope of the decreasing field on the strain-electric field curve.

**We replaced $\langle hkl \rangle$ with $[hkl]$ because it more accurately represents the measured property.

high aspect ratios to produce smaller grain sizes, higher texture qualities, and improved properties. Highly [001]_c oriented PMN-PT ceramics with $f_{(001)} \sim 0.94$ – 0.99 were produced by Richter et al.⁸⁸ using 5 vol% fine BT templates (~ 10 μm), and a d_{33}^* value of 877 pm/V was obtained. Yan et al.⁸⁹ textured PMN-PT with $f_{(001)}$ of 0.98 using 1 vol% fine BT templates. A static d_{33} of 1000 pC/N and a T_c of 162 °C were achieved. BT template particles do not react with the PMN-PT matrix and thus remain as residual inclusions in the textured ceramics, and, as a result, reduce both the strain response of the ceramics via mechanical clamping, and the dielectric properties via a composite effect. Brosnan et al.⁹⁰ found that using SrTiO₃ templates can eliminate this problem and yield higher piezoelectric response (static $d_{33} = 940$ pC/N), as the SrTiO₃ templates dissolve into

bulk PMN–PT. However, Sr^{2+} lowers the Curie temperature of PMN–PT to 103 °C. Amorin et al.⁹¹ showed that PMN–PT particles can be used as templates in PMN–PT to avoid both of these issues, but the templates were low aspect ratio and thus could not be efficiently aligned during fabrication. Recently, 5–15 μm NBT–PT platelets were used to template PMN–PT.⁹² Since these templates form a solid solution with PMN–PT, they result in high density and fine grain size ($\sim 10 \mu\text{m}$) ceramics with excellent texture quality ($f_{001} \sim 0.92$), high piezoelectricity ($d_{33} = 1016 \text{ pC/N}$) and a Curie temperature of 129 °C.

$[001]_c$ textured rhombohedral PMN–PT near the MPB showed high piezoelectric properties, but the low rhombohedral to tetragonal phase transition temperature (T_{r-t}) and low Curie temperature (T_c , ~ 90 – 170 °C) limit the working temperature. Tetragonal PMN–PT compositions distant from the MPB have higher Curie temperatures than rhombohedral PMN–PTs and thus there is no intermediate ferroelectric–ferroelectric phase transition. $[111]$ oriented BT templates were used to texture tetragonal PMN–40PT ceramics, with an $f_{(111)}$ of 0.95.⁹³ The textured PMN–40PT ceramics exhibited excellent piezoelectric properties between room temperature and the Curie temperature (205 °C).

Extensive effort has focused on texturing new systems with higher T_{r-t} and T_c , including modified PT,⁹⁴ PIN–PMN–PT,^{95,96} $\text{Pb}(\text{Yb}_{1/2}\text{Nb}_{1/2})\text{O}_3$ – $\text{Pb}(\text{Mg}_{1/3}\text{Nb}_{2/3})\text{O}_3$ – PbTiO_3 (PYN–PMN–PT),⁹⁷ and $\text{Pb}(\text{Mg}_{1/3}\text{Nb}_{2/3})\text{O}_3$ – $\text{Pb}(\text{Zr,Ti})\text{O}_3$ (PMN–PZT).^{98,99} $[001]_c$ oriented Sm- and Mn-modified PbTiO_3 ceramics textured to $f_{(001)} = 0.95$ with 5 wt% NBT–PT were shown to have a T_c of 364 °C, a d_{33} of 127 pC/N and an large g_{33} ($115 \times 10^{-3} \text{ V m N}^{-1}$).⁹⁴ The authors hypothesized that self-polarization due to grain orientation along the spontaneous polarization direction plays an important role in achieving a large piezoelectric response in domain motion-confined materials. High piezoelectric properties (static d_{33} of 824 and 780 pC/N) and substantially improved phase transition temperatures (~ 20 – 70 °C greater than PMN–PT) were demonstrated for $[001]_c$ textured PIN–PMN–PT ($f_{(001)}$ of 0.90),^{95,96} templated with 5 vol% BT templates. Textured PIN–PMN–PT showed significantly improved strain versus field behavior relative to equiaxed ceramic and approach those of the single crystal (Fig. 11).¹⁰⁰ Also, the coercive field of 8.3 kV/cm is much higher than that obtained with binary PMN–PT ceramics. Similar to PIN–PMN–PT, $[001]_c$ textured PIN–PMN–PT ceramics with $f_{(001)}$ of 0.91 show a high level of strain (0.33%) and a higher T_c of 214 °C.⁹⁷ Yan et al. fabricated textured PMN–PZT ceramics with $f_{(001)}$ of 0.90 and $f_{(111)}$ of 0.72 using (001) and (111) BT templates, respectively.^{98,99} In addition to the higher T_c of 204 °C, $[001]_c$ textured PMN–PT possessed a very high energy density of $d_g = 59,000 \times 10^{-15} \text{ m}^2/\text{N}$, which is comparable to that of the

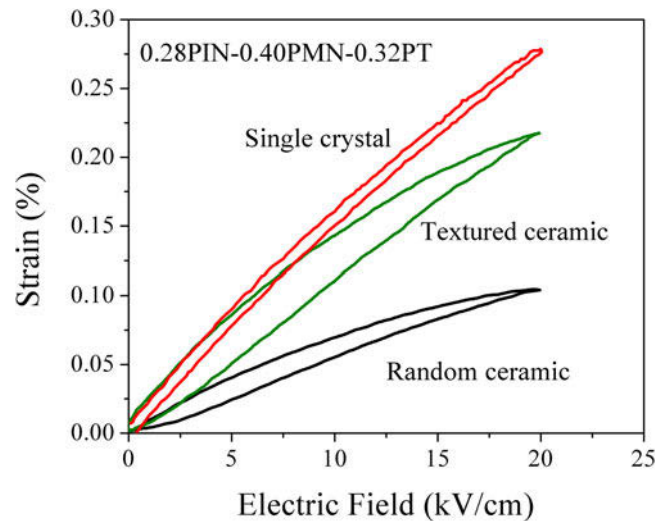


FIG. 11. Comparison of the high field response of $[001]_c$ textured 0.28PIN–0.40PMN–0.32PT ceramic with untextured ceramic and single crystal.¹⁰⁰

single crystal counterpart and 359% higher than that of the best commercial ceramics. $[111]$ textured ceramics exhibited much higher piezoelectric anisotropic factor d_{15}/d_{33} of 8.5 (versus 2.0 in the untextured counterpart), indicating “rotator” ferroelectric characteristics wherein the large shear piezoelectric response contributes longitudinal piezoelectric response in the non-polar direction ($d_{33} = 1100 \text{ pC/N}$ in $[001]$ textured ceramics versus $d_{33} = 112 \text{ pC/N}$ in $[111]$ textured ceramics).⁹⁹

C. Lead-free piezoelectrics

For environmental reasons, there is tremendous interest in the development of lead-free piezoelectric ceramics as replacements for lead-based ceramics. Texture control is an important approach to enhance piezoelectric properties in lead-free ceramics. (K,Na) NbO_3 -based, $\text{Bi}_{1/2}\text{Na}_{1/2}\text{TiO}_3$ -based and BaTiO_3 -based ceramics are the primary lead-free textured piezoelectric ceramics under investigation owing to higher piezoelectric properties relative to other compositions.

D. Textured (K,Na) NbO_3 -based piezoelectrics

The (K,Na) NbO_3 -based system is considered to be a very promising candidate for lead-free piezoelectrics due to the high Curie temperatures and ferroelectric properties. Since the pioneering work of Saito et al., this system has become one of the most investigated textured piezoelectrics of the last decade.¹⁰¹ They reported that the combination of texture-engineering through RTGG and compositional design (Li^+ , Ta^{5+} , and Sb^{5+} co-substitutions) results in a high piezoelectric coefficient of 416 pC/N, comparable to untextured commercial PZT ceramics. The Li^+ , Ta^{5+} , and Sb^{5+} co-substitutions alter

the phase structure of KNN and shift the polymorphic phase transition (PPT) temperature from about 200 °C to near room temperature.^{102–105} This PPT shift not only enhances the room temperature piezoelectric response of the ceramics, but also results in a substantial increase in the temperature dependence of the piezoelectric properties. Since many applications require a stable piezoelectric response over a wide temperature range, subsequent studies focused on texturing KNN-based systems with a PPT far above room temperature. Low concentrations of CuO dopants, or Li⁺, Ta⁵⁺, and Sb⁵⁺ substitutions, were added to KNN to aid in densification and texture development, and the ceramics were fabricated by TGG or RTGG with $f_{(001)}$ as high as 0.97.^{106–112} The modified ceramics show d_{33} of ~146–218 pC/N, with a PPT above 150 °C. Tutuncu et al.¹¹³ used *in situ* X-ray diffraction to observe nucleation, texture development, and phase equilibria during TGG of Li⁺ doped KNN. Table II summarizes the piezoelectric properties of this class of textured ceramics as a function of texturing approach and texture fraction.

E. Textured Bi_{1/2}Na_{1/2}TiO₃-based piezoelectrics

Bi_{1/2}Na_{1/2}TiO₃ (BNT) and Bi_{1/2}K_{1/2}TiO₃ (BKT) are important end members of a variety of piezoelectric solid solution compositions. These ceramics, such as BNT–BKT, BNT–BT, BKT–BT, and BNT–BKT–BT, form MPBs with enhanced piezoelectric properties relative to the end members. Various templates, such as KSr₂Nb₅O₁₅ (KSNO), SrTiO₃ (ST), Bi₄Ti₃O₁₂ (B4TO), H_{1.07}Ti_{1.73}O₄·*n*H₂O (HTO), NaNbO₃ (NN), SrBi₄Ti₄O₁₅ (SBTO), Al₂O₃ and TiO₂, were used to texture [001]_c oriented BNT and BKT-based ceramics.^{114–122} Although highly textured BNT-based ceramics were fabricated, significant improvements in piezoelectric properties were precluded because of residual templates with little or no piezoelectric activity. Later, researchers synthesized BNT platelets to texture BNT-based ceramics.^{123–126} The piezoelectric response increased substantially with increasing texture and the textured ceramic had a d_{33} of 322 pC/N, or ~200% higher than untextured ceramics. However, the depolarization temperature of the ceramics was not substantially reduced.^{123,124}

F. Textured BaTiO₃-based piezoelectrics

BaTiO₃, with a Curie temperature of ~120 °C and a d_{33} coefficient of ~190 pC/N, is also a very promising lead-free candidate. TGG, RTGG and magnetic alignment have been used to fabricate [001]_c, [110]_c and [111]_c oriented BT. Recent studies are summarized in Table II. Vriami et al.¹²⁷ and Fu et al.¹²⁸ fabricated [001]_c textured BT ceramics with [001] BT templates, and found that samples with an $f_{(001)}$ of 0.97 have a d_{33} of 274 pC/N. For a [110] grain oriented BaTiO₃,¹²⁸ the piezoelectric

constant d_{31} was unchanged at 50 pC/N, while the d_{33} was 788 pC/N at $f_{(110)} = 0.85$. [111] oriented BT ceramics with $f_{(111)}$ of ~0.66 and $f_{(001)}$ of 0.95 were fabricated with [111] BT and [001] NaNbO₃ templates, respectively.^{129,130}

A and B site substituted BT such as (Ba,Ca)TiO₃ (BCT), Ba(Zr,Ti)O₃ (BZT), (Ba,Ca)(Zr,Ti)O₃ (BCZT) and (Ba,Ca)(Ti, Sn)O₃ (BCST) have received much attention since Ren et al.¹³¹ reported that a d_{33} of about 620 pC/N can be achieved in untextured BCZT ceramics. Texturing of substituted BT-based ceramics did show some improvements in piezoelectric properties, possibly being facilitated by enhanced polarization switching.^{132–137} However, their d_{33} values are still lower than that achieved in randomly oriented BCZT ceramics. Ye et al.¹³⁸ suggested that this can be caused by the lower sintered density due to the introduction of BT or CT templates.

G. Textured bismuth-layered piezoelectrics

Bismuth-layered ceramics are of interest for high temperature and high power piezoelectric applications because they possess a high T_c and Q_m .¹³⁹ The bismuth-layered structure, also known as the Aurivillius structure, is a class of materials composed of layers of pseudo-perovskite unit cells of (A_{*m*-1}B_{*m*}O_{3*m*+1})²⁻ layers separated by (Bi₂O₂)²⁺ layers oriented in the *a*–*b* plane. The term *m* represents the number of octahedral B-sites that lie along the [001] direction between the (Bi₂O₂)²⁺ layers.¹⁴⁰ A number of bismuth-layered structure ceramics, such as Bi₄Ti₃O₁₂ (BIT), SrBi₄Ti₄O₁₅ (SBT),¹⁴¹ SrBi₂Nb₂O₉ (SBN), and CaBi₄Ti₄O₁₅ (CBT),¹⁴² have been textured by TGG and spark plasma sintering.^{139,143} To date these materials have significantly lower piezoelectric properties than lead-based and other lead-free textured piezoelectrics (Table SI).^{139–147}

H. Textured tungsten-bronze piezoelectrics

Tungsten-bronze type materials, such as Ba₂NaNb₅O₁₅ (BNN),¹⁴⁸ KSr₂Nb₅O₁₅ (KSN),¹⁴⁹ and Sr_{0.5}Ba_{0.5}Nb₂O₆ (SBN),¹⁴⁹ have d_{33} values that are up to an order of magnitude higher than in textured Aurivillius phase materials. Efforts to texture-engineer tetragonal tungsten-bronze ceramics, including Ba₂NaNb₅O₁₅ (BNN)¹⁴⁸ and KSr₂Nb₅O₁₅ (KSN) take advantage of the acicular morphology of BNN, KSN and KNN templates that form during molten salt synthesis.¹⁵⁰ In all cases, high degrees of template alignment were achieved by extrusion, gated doctor blading and magnetic alignment. In most cases, there were significant gains in d_{33} relative to untextured ceramics, but the piezoelectric properties are significantly less than lead-based and other lead-free textured piezoelectrics (Table SII).^{148–155}

VIII. TEXTURED CERAMICS FOR OPTICAL APPLICATIONS

Most optical applications require materials that are transparent, or at least translucent. Transparency in ceramics is achieved by limiting sources of scattering, absorption, and reflection of photons. Cubic ceramics like spinel (MgAl_2O_4) and yttrium aluminum garnet ($\text{Y}_3\text{Al}_5\text{O}_{12}$, YAG) can achieve high transparency in a randomly oriented polycrystalline state, since there is no refraction when light passes from one grain to another (i.e., the refractive index in cubic materials is isotropic) regardless of the crystallographic orientation change from one grain to the other. The same is not true of non-cubic materials (e.g., alumina) and refraction at grain boundaries has a significant effect on reduced transparency due to refractive index anisotropy in different crystallographic directions. For this reason, efforts have been made to fabricate textured optical ceramics such that the grains are oriented in the transmission direction.

It should be noted that the optical transmission, T_{th} , of anisotropic ceramics can be improved by limiting the grain size to ≤ 200 nm (the short wave length end of the visible light spectrum).¹⁵⁶ For example, 0.8 mm thick alumina plates with an average grain size of 300 nm had 83% T_{th} at a wave length of 620 nm. Further improvements require texture-engineered ceramics, in which the alignment of the crystalline orientation minimizes or eliminates scattering due to crystallographic misalignment (i.e., refractive index differences) between grains.

Magnetic alignment of alumina at 12 T, yielded 60–65% transmission at 600 nm for textured alumina with grain sizes in the tens of microns and a $f_{(001)}$ of 0.45.^{5,157} The highest reported in-line transmission of 91% T_{th} was reported for a textured alumina with a grain size of 100–

500 nm, but the degree of crystallographic texture was not measured.¹⁵⁸

Tetragonal strontium barium niobate, $\text{Sr}_{0.6}\text{Ba}_{0.4}\text{Nb}_2\text{O}_6$ (SBN60) was textured by Tanaka et al. using magnetic alignment to enhance the electro-optical properties relative to untextured ceramics.¹⁵⁹ Similar compositions have been textured using TGG, but not to transparency. The Tanaka et al. paper is the first report of a highly translucent textured polycrystalline SBN60 (58% T_{th}). Figure 12 illustrates the significant improvement in optical transmittance achieved by texturing SBN60. The authors measured an apparent electro-optic coefficient of 342 pm/V for the textured material, or $\sim 95\%$ of the value for single crystal SBN60, and thirteen orders of magnitude higher than untextured SBN ceramics.

Rare earth-doped fluorapatite ($\text{RE}:\text{Ca}_{10}(\text{PO}_4)_6\text{F}_2$ or RE:FAP), with a hexagonal crystal structure, has the potential to yield higher power lasers at room temperature, which is a great advantage over RE-YAG gain media which operate at cryogenic temperatures.¹⁶⁰ The rare earth dopants (e.g., Nd^{3+} , Yb^{3+}) necessary for lasing fortuitously enhance the magnetic anisotropy of these materials and thus particles can be aligned at < 2 T, which is much closer to a manufacturing reality because rare earth magnets can be used for processing. Textured Nd:FAP,^{160,161} and Yb:FAP¹⁶² were both demonstrated to be laser grade, but texture quality was not measured or analyzed in these materials. The application of textured ceramics in such a demanding application is considered to be a major advance for laser media ceramics.

An interesting phenomenon with regard to Nd:YAG ceramic materials is thermal birefringence-induced depolarization. Even though YAG is optically isotropic under ambient conditions, a slight birefringence occurs in laser gain media during use, reducing the lasing efficiency of the material.¹⁶³ Similar losses occur in single crystal media cut in the [111] direction. The losses due to anisotropic dependence of lasing efficiency on crystallographic orientation were reduced by more than 90% by cutting the crystals in the [110] direction.¹⁶⁴ This suggests that the lasing efficiency of YAG ceramics

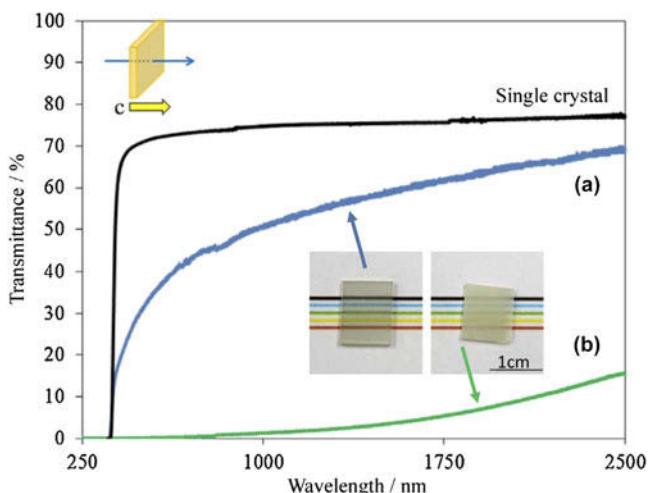


FIG. 12. Transmittance data for (a) textured ceramic and (b) untextured ceramic SBN60 relative to a SBN60 single crystal. Reproduced with permission from Ref. 159.

TABLE III. Optical transmission and texture quality of magnetically oriented textured ceramics.

Material	Transmission/thickness (% T_{th} at 600 nm/mm)	Lotgering factor ($f_{(00n)}$)	Magnetic field (T)
Al_2O_3 (Ref. 5)	64/0.8	*	10
Al_2O_3 (Ref. 157)	60/1	0.45	12
$\text{Al}_2\text{O}_3^\wedge$ (Ref. 158)	91/0.8	*	10
$\text{Sr}_{0.6}\text{Ba}_{0.4}\text{Nb}_2\text{O}_6$ (Ref. 159)	58/1	0.85	10
Nd:FAP ¹⁶¹	*/0.47	0.96	1.4
Yb:FAP ¹⁶²	*/0.6	0.90	1.7

*—Not reported, \wedge —grain size 100–500 nm.

could be improved by [110] texturing. A unique process for orienting YAG reported by Arakawa et al.,¹⁶⁵ takes advantage of the phase reactions between Y_2O_3 and Al_2O_3 to produce textured YAG. The process involves spin coating a sol-gel yttria precursor onto either (0001) or (1120) sapphire with a subsequent heat treatment at ~ 1600 °C to achieve a pure YAG film with a Lotgering factor of up to 0.57 on (0001) sapphire and 0.23 on (1120) sapphire. The [211] direction was parallel to the growth direction of the YAG film on the (0001) sapphire crystal, with an epitaxial relationship between the substrate and film, while no epitaxial relationship was seen in the film grown on the (1120) sapphire crystal. While this technique is still in the early stages of development and has only been reported for a relatively large single crystal sapphire substrate, it opens the door to RTGG of YAG using alumina platelets and an yttria/alumina mixture matrix. The transmittance and texture quality data for the materials described above are summarized in Table III.

IX. TEXTURED THERMAL CONDUCTORS

In ceramics, heat is transported by phonons and the thermal conductivity of ceramics is determined by crystallographic factors such as bond strength, atomic weight, atomic coordination, and complexity of the unit cell.^{166,167} Materials with strong (covalent) bonds, low atomic weights, tetrahedral coordination of the atoms, and simple crystal structures are typically good phonon conductors and have high thermal conductivities. Therefore, inexpensive non-oxide ceramics, such as SiC, AlN, and Si_3N_4 (alpha and beta) are used in commercial applications, for example as heat sinks in the electronics industry.

SiC, AlN, and Si_3N_4 have anisotropic crystal structures, which result in anisotropic thermal conductivities. For AlN and SiC this crystallographic anisotropy is small, i.e., the ratio of thermal conductivity along the *c*-axis and along the *a/b*-axes is about 1.5, which suggests that little improvement is expected through texturing. For textured AlN with a Lotgering factor of 0.76, only a small anisotropy in thermal conductivity of 164.7 W/(K m) parallel and 154.6 W/(K m) perpendicular to the direction of alignment

was observed.¹⁶⁸ Others reported similar trends with Lotgering factors between 0.6 and 0.97 and measured thermal conductivities of 86.3 W/(K m) parallel and 83.7 W/(K m) perpendicular to the direction of alignment.¹⁶⁹

In contrast, β - Si_3N_4 consists of a network of corner-shared Si-N₄ tetrahedra that form channels parallel to the *c*-axis. Molecular dynamics calculations predict thermal conductivities of 450 W/(m K) and 170 W/(m K) along the *c*- and *a*-axes, respectively, in single crystals.¹⁶⁷ Measured thermal conductivities of β - Si_3N_4 single crystals of 180 W/(m K) along the *c*-axis and 69 W/(m K) along the *a*-axis were reported.^{166,170} The experimental values are lower than the predicted single crystal values because of defects such as impurities, vacancies and dislocations.

Textured β - Si_3N_4 was produced by slip casting under a magnetic field,^{171,172} tape casting,^{170,173} and extrusion.¹⁷⁴ The highest degree of texture, with an $f_{(001)}$ of 0.98, was obtained by slip casting at 12 T (Fig. 13),¹⁷² resulting in a thermal conductivity of 176 W/(m K) along and 62 W/(m K) perpendicular to the grain alignment direction, whereas the thermal conductivity of untextured β - Si_3N_4 is ~ 115 W/(m K).

X. TEXTURED STRUCTURAL CERAMICS

Structural ceramics exhibit high elastic moduli, high hardness and wear resistance. However, brittleness (i.e., low resistance to the propagation of cracks) and strength variability (due to extrinsic defects in the material) compromise their use. The brittle fracture in ceramics is associated with low energy dissipation during fracture. Improvements in the fracture resistance can be ascribed to morphological phenomena such as grain bridging, interfacial bonding, as well as energy dissipating mechanisms acting during crack propagation (e.g., crack deflection, delamination).

A primary motivation for texturing structural ceramics is to enhance wear resistance by increasing the material's hardness. There is a significant difference in the hardness of single crystals compared to polycrystalline ceramics. For example, Vicker's hardness perpendicular to the

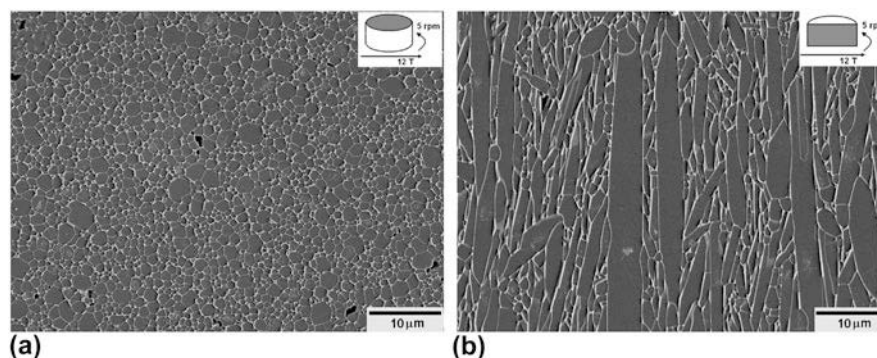


FIG. 13. SEM micrographs of polished and plasma etched surfaces of textured β - Si_3N_4 . Reproduced with permission from Ref. 172.

basal surface (0001) in single crystal alumina is 23.0 GPa, while polycrystalline alumina samples commonly exhibit a hardness of 19.0 GPa, as reported by McColm.¹⁷⁵ To date the data on hardness of single crystal sapphire and textured ceramics is quite variable; a problem associated with proper measurements of hardness. For example, Carisey et al. showed that the hardness of textured alumina perpendicular to the [0001] texture direction is 16.5 GPa compared to 16 GPa for untextured alumina.¹⁷⁶

The hardness of single crystal β - Si_3N_4 is 34.4 GPa perpendicular to the (0001) surface.¹⁷⁵ Nakamura et al.¹⁸⁴ studied the hardness anisotropy in textured β - Si_3N_4 fabricated by extrusion and reported hardnesses of 17.0 GPa perpendicular to the (0001) surface and 12.6 GPa parallel to this surface. In this same work the hardness of untextured β - Si_3N_4 polycrystalline material was 15.6 GPa.

Single crystal silicon carbide exhibits a hardness of 33.0 GPa perpendicular to the (0001) surface, while untextured polycrystalline SiC has an isotropic hardness of 19.3 GPa.¹⁷⁵ Work by Lee et al. on hot-forged SiC found the hardness on the (0001) surface to be 24.4 GPa while the hardness perpendicular [0001] direction was 26.8 GPa.¹⁷⁷

Residual microstresses generated in the ceramic during cooling after sintering are affected by the anisotropic coefficient of thermal expansion and orientation of the grains. For instance, the thermal expansion anisotropy of single crystal Al_2O_3 is $7.2 \times 10^{-6} \text{ }^\circ\text{C}^{-1}$ in the [0001] direction and $6.3 \times 10^{-6} \text{ }^\circ\text{C}^{-1}$ in the $[\bar{1}2\bar{1}0]$ direction. Residual stresses can be reduced in textured materials by aligning grains. For example, Vedula et al. predicted residual stresses (maximum principal stresses, σ_{11}) after sintering to be ~ 530 MPa for untextured alumina compared to ~ 415 MPa in [0001] textured alumina.¹⁷⁸

Regarding the fracture behavior of single crystal alumina, toughness anisotropy depends on the different cleavage energy of crystallographic planes. According to Salem et al., the basal (0001) plane of an alumina single crystal showed a 45% higher resistance toward cleavage than the prism planes of the crystal structure, measured using the chevron notch method.¹⁷⁹ Interestingly, magnetic field [001]-oriented 3 mol% yttria stabilized tetragonal zirconia had an indentation fracture toughness in [001] direction that was 54% higher than in the perpendicular direction, and 49% higher than that of untextured zirconia.¹⁸⁰ These findings suggest that texturing microstructures in polycrystalline ceramics can be effective if properly oriented with respect to the applied load. Nevertheless, not only the crystallographic texture but also the morphology of the textured microstructures (e.g., elongated grains with high aspect ratio) may influence the fracture behavior of polycrystalline ceramics. For example, Pavlacka and Messing textured alumina by TGG, obtaining a [0001]-fiber textured material (Fig. 1).¹⁸⁷

They reported indentation-strength effective toughness values of $4.58 \text{ MPa m}^{1/2}$ when measured parallel to the basal surface of [0001] oriented alumina and $2.55 \text{ MPa m}^{1/2}$ when measured perpendicular to the basal surface. In this work, the property anisotropy is due to the of crack propagation behavior. In each crack mode, the crack is macroscopically straight, which indicates that there is no difference in the tortuosity of the crack path. The difference between the two crack modes, and thus the origin of this property anisotropy, is the ability of the crack to travel through an oriented grain. As discussed above, the hardness of alumina is higher parallel to the basal surface than perpendicular to it. Therefore the crack is more likely to travel through grains when toughness is measured perpendicular to the basal surface than when it is measured parallel to the basal surface. This finding indicates that texturing structural ceramics using TGG can also increase the fracture energy of the material, thus enhancing the damage tolerance of the final ceramic part.

In an untextured polycrystalline ceramic, crack propagation usually follows a path perpendicular to the applied stress field (mode I fracture). In contrast, textured ceramics, such as textured α -alumina, can affect the direction of crack propagation due to the relatively low fracture energy of the interfaces between templated grains, thus promoting delamination.^{181–186} The competition between crack penetration and delamination in a textured material can be described by the energy-based model illustrated in Fig. 14(a), which is based upon the He and Hutchinson criterion for cracks propagating in bimetals.¹⁸³ In this figure, regions for penetration through the textured grain or deflection along the interfaces between oriented tabular grains are schematically illustrated. Figure 14(a) shows the two modes of crack propagation possible between “brick-like” textured grains. The curve G_d/G_p represents the ratio between the critical energy release rate of the potential deflected crack (G_d) and the critical energy release rate of the potential penetrating crack (G_p). In monolithic structural ceramics there is, in general, little mismatch in the Young’s moduli between grains ($\alpha \approx 0$) and the crack deflects if the interfacial fracture resistance (Γ_i) is less than 25% of the fracture resistance of the grain (G_c) (i.e., $\Gamma_i/G_c \leq 0.25$). Both G_c and Γ_i can be influenced by the anisotropy of the crystal.^{181,182} Measurements of interfacial fracture toughness, Γ_i , of textured alumina compared to the fracture energy in untextured alumina, G_c , resulted in $\sim 1/3$ [represented in Fig. 14(a) by the solid symbol], showing the potential of texturing for favoring delamination, and thus enhanced energy dissipation.¹⁸¹

To increase the capability of a textured microstructure to deflect a propagating crack a novel approach was proposed using layered ceramics with compressive residual stresses.¹⁸² This concept was demonstrated in an alumina-based layered ceramic with textured layers

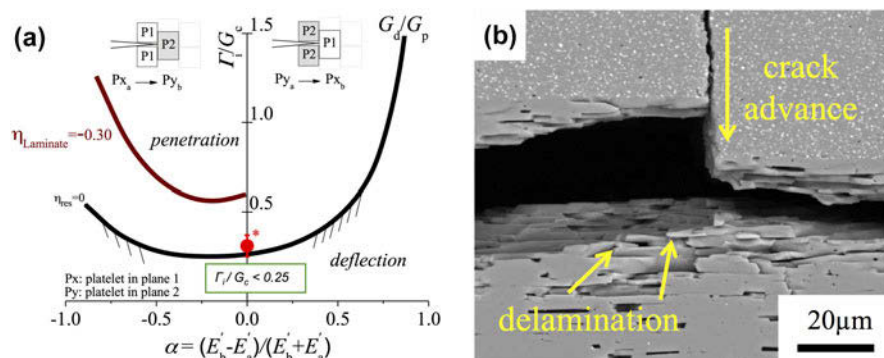


FIG. 14. (a) Model to predict crack deflection or penetration in textured microstructures with and without residual stresses. The curve G_d/G_p represents the ratio between the critical energy release rate of the potential deflected crack (G_d) and the critical energy release rate of the potential penetrating crack (G_p). The large dot on the y axis is the ratio of interfacial fracture resistance between two templates and the fracture resistance of the grain, i.e., Γ_i/G_c . (b) SEM micrograph showing the crack path (delamination) within a textured layer under compressive stress. Reproduced with permission from Ref. 181.

embedded between layers of equiaxed alumina. The textured layers consist of alumina grains aligned parallel to the layer plane. Due to the different coefficients of thermal expansion of the layers, tensile and compressive residual stresses develop in the equiaxed and textured layers, respectively. According to He and Hutchinson, the incorporation of compressive residual stresses shifts the G_d/G_p curve upwards, thus promoting delamination [see Fig. 14(a)]. Figure 14(b) shows a typical crack path within the textured layer designed with compressive stresses. It is demonstrated that the combination of compressive residual stresses in textured layers together with the relatively low interfacial energy between the basal planes of the oriented alumina grains favor delamination, thus increasing the overall toughness of the system.

MAX phases are ternary nitrides and carbides with the general formula $M_{n+1}AX_n$, where M is an early transition metal, A is an A group element (columns 13–16 in the periodic table), and X is carbon or nitrogen, with $n = 1–3$. MAX phases have received a lot of attention due to their unique combination of high elastic constants of 178–340 GPa, high hardnesses of 1.4–8 GPa, compressive strengths of up to 1.9 GPa, and a fracture toughnesses of 4.5–16 $\text{MPa m}^{1/2}$.¹⁸⁸ MAX phases even show some degree of plasticity, which makes them machinable and resistant to thermal shock. MAX phases have a layered hexagonal crystal structure (space group $P6_3/mmc$) and consist of alternate near-close-packed layers of edge sharing M_6X octahedra and layers of A atoms in between those layers.¹⁸⁸

MAX phase crystals grow preferentially along the basal plane to form platelets, which suggests that a significant improvement of properties can be expected by texturing. Ti_2AlC , Ti_3SiC_2 , Ti_3AlC_2 , and Nb_4AlC_3 have been textured by hot pressing,¹⁸⁹ slip casting under a magnetic field,^{190–195} electrophoretic deposition,¹⁹⁶ and spark plasma sintering.^{197,198} Spark plasma sintering,

hot pressing, and electrophoretic deposition under a magnetic field produce textures with Lotgering factors ($f_{(001)}$) of 0.69–0.75 and the mechanical properties of the samples are somewhat improved compared to untextured ceramics.^{197,198} Highly textured MAX phases produced by slip casting under a magnetic field have a $f_{(001)}$ of 0.95–0.97 and significantly improved properties.^{190–195} For high Lotgering factors of 0.97, the bending strength and fracture toughness of Nb_4AlC_3 was improved to 1219 MPa and 17.9 $\text{MPa m}^{1/2}$, respectively.¹⁹² It is interesting to note that the mechanical properties improved both parallel and perpendicular to the orientation direction, e.g., the flexural strength of isotropic polycrystalline Ti_3AlC_2 is 320 MPa, but textured Ti_3AlC_2 with an $f_{(001)}$ of 0.69 has a flexural strength of 1261 MPa parallel and 1005 MPa perpendicular to the texturing direction.¹⁹⁵ A significant improvement of the fracture toughness from 6.9 $\text{MPa m}^{1/2}$ for isotropic Ti_3AlC_2 ceramics to 13.1 $\text{MPa m}^{1/2}$ parallel and 14.6 $\text{MPa m}^{1/2}$ perpendicular to the texturing direction was also reported.¹⁹⁵

XI. FUTURE DIRECTIONS IN TEXTURE-ENGINEERED CERAMICS

There have been major advances in tailoring the piezoelectric and thermoelectric properties of bulk ceramics through crystallographic texturing and thus some of the materials discussed above are promising candidates for future commercialization. A few papers demonstrate that there are enormous opportunities for enhanced properties in textured optical, ionic conducting, structural and thermal ceramics. There is surprisingly little fundamental research on the physics of texture-property relations which points to a need for basic research to understand how fundamental material properties correlate with texture quality.

The texture fractions resulting from most fabrication techniques are $>95\%$, and thus texture fraction is not believed to be the property-limiting factor. However, the alignment of the grains is problematic because the degree of misorientation in the orientation distribution function limits the property values that can be achieved. For example, as predicted for piezoelectric materials, a misalignment of 10° reduces the d_{33} by $>25\%$ compared to the single crystal values.¹⁹⁹ Current research on texture-engineered ceramics demonstrates that there is considerable room for improvement in the uniaxial alignment by TGG and magnetic alignment. This is especially evident when the FWHM of textured bulk ceramics is compared to the $<1^\circ$ FWHM achieved by various thin film growth processes and the RABiTS process. In contrast, the best orientation achieved by TGG ranges from 5 to 20° FWHM.^{14,200} Recently, we showed that combining magnetic alignment of template particles and TGG resulted in a FWHM of 5° .²⁰¹ High field magnetic alignment alone yields a FWHM of 8 – 12° .

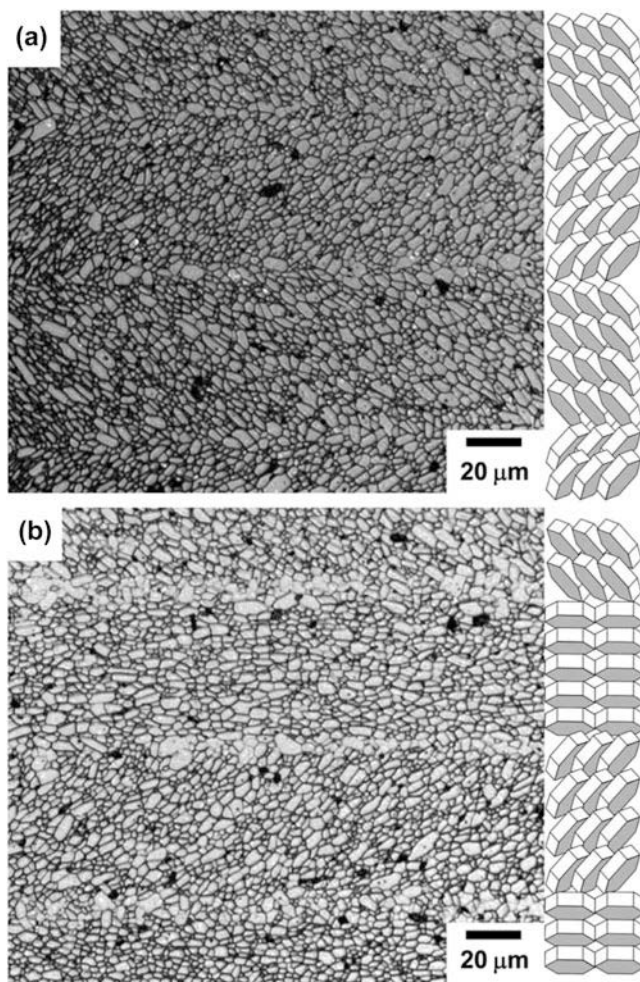


FIG. 15. Microstructures of lamina alumina composites prepared by altering the direction of the electric field relative to the magnetic field during electrophoretic deposition in a strong magnetic field. Reproduced with permission from Ref. 17.

Most of the fabrication techniques reported in the literature result in fiber-textured ceramics. Processing methods that produce biaxially-textured ceramics with orientation distributions similar to that of thin films would be a major advance in the field of texture-engineered ceramics. We expect that the properties of biaxially textured ceramics with a narrow orientation distribution would approach those of single crystals. Additionally, novel orientation patterns, such as seen in Fig. 15, have the potential to yield properties that are not seen in single crystals or traditionally textured materials.¹⁷ Further study of texturing ceramics with $[111]$ and $[011]$ textures would likewise advance the potential of textured ceramics.

Current magnetic alignment and TGG processes are still batch processes. In the case of magnetic alignment, the use of a high field (10 T) is problematic. While TGG-type processes build on existing tape casting, and other scalable powder processes, lack of commercial sources of anisotropic templates by design (e.g., size, composition, aspect ratio and crystallographic orientation) have slowed commercialization. Clearly, there is a need to engineer these processes and to develop new methods to overcome the limitations of existing textured ceramics fabrication processes.

An important challenge in future texture-engineered ceramics research is to determine how to quantify texture fraction and the orientation distribution so that properties can be better correlated with texture. As reported by Jones et al., the Lotgering factor, texture fraction, and orientation parameters from the March–Dollase equation are insufficient for establishing accurate and comprehensive correlations of texture quality and properties.²⁰² A coupled issue is how to utilize the enormous data sets obtained with various texture analysis tools. Such challenges need to be overcome so that we can test theory and establish new structure–property relations for textured ceramics.

Finally, there is little fundamental understanding about texture evolution as a function of template–matrix interactions, grain growth, and interactions between growing grains. A comprehensive analysis of texture evolution by *in situ* techniques would provide valuable insights into how process parameters can be used to obtain high quality textured ceramics. Finally, we believe that texture-engineered ceramics hold much promise and that their development will expand the commercial applications of ceramic materials and facilitate greater understanding of the link between grain orientation and properties.

REFERENCES

1. G.W. Rathenau, J. Smit, and A.L. Stuyts: Ferromagnetic properties of hexagonal iron-oxide compounds with and without a preferred orientation. *Z. Physik* **133**, 250 (1952).

2. G.L. Messing, T. Trolrier-McKinstry, E.M. Sabolsky, C. Duran, S. Kwon, B. Brahmarrout, P. Park, H. Yilmaz, P.W. Rehrig, K.B. Eitel, E. Suvaci, M. Seabaugh, and K.S. Oh: Templated grain growth of textured piezoelectric ceramics. *Crit. Rev. Solid State Mater. Sci.* **29**, 45 (2004).
3. S. Jin and J.E. Graebner: Processing and fabrication techniques for bulk high- T_c superconductors: A critical review. *Mater. Sci. Eng., B* **7**, 243 (1991).
4. E. Guilmeau, H. Itahara, T. Tani, D. Chateigner, and D. Grebille: Quantitative texture analysis of grain-aligned $(\text{Ca}_2\text{CoO}_3)_{0.62}\text{CoO}_2$ ceramics processed by the reactive-templated grain growth method. *J. Appl. Phys.* **97**, 064902 (2005).
5. X. Mao, S. Wang, S. Shimai, and J. Guo: Transparent polycrystalline alumina ceramics with orientated optical axes. *J. Am. Ceram. Soc.* **91**, 3431 (2008).
6. H. Imamura, K. Hirao, M.E. Brito, M. Toriyama, and S. Kanzaki: Further improvement in mechanical properties of highly anisotropic silicon nitride ceramics. *J. Am. Ceram. Soc.* **83**, 495 (2000).
7. G.E. Youngblood and R.S. Gordon: Texture-conductivity relationships in polycrystalline lithia-stabilized β'' -alumina. *Ceramurgia Intl.* **4**, 93 (1978).
8. A.H. Heuer, D.J. Sellers, and W.H. Rhodes: Hot-working of aluminum oxide: I. Primary recrystallization and texture. *J. Am. Ceram. Soc.* **52**, 468 (1969).
9. A. Carman, E. Pereloma, and Y. Chen: Hot forging of a textured α -SiAlON ceramic. *J. Am. Ceram. Soc.* **89**, 478 (2006).
10. J.J. Went, G.W. Rathenau, E.W. Gorter, and G.W. van Oosterhout: Hexagonal iron-oxide compounds as permanent-magnet materials. *Phys. Rev.* **86**, 424 (1952).
11. A. Goyal, R. Feenstra, F.A. List, M. Paranthaman, D.F. Lee, D.M. Kroeger, D.B. Beach, J.S. Morrell, T.G. Chirayil, D.T. Verebelyi, X. Cui, E.D. Specht, D.K. Christen, and P.M. Martin: Using RABiTS to fabricate high-temperature superconducting wire. *JOM* **51**, 19 (1999).
12. S. Jin, R.C. Sherwood, R.B. van Dover, T.H. Tiefel, and D.W. Johnson, Jr.: High T_C superconductors-composite wire fabrication. *Appl. Phys. Lett.* **51**, 203 (1987).
13. T. Tani: Texture engineering of electronic ceramics by the reactive-templated grain growth method. *J. Ceram. Soc. Jpn.* **114**, 363 (2006).
14. H. Yilmaz, G.L. Messing, and S. Trolrier-McKinstry: (Reactive) templated grain growth of textured sodium bismuth titanate $(\text{Na}_{1/2}\text{Bi}_{1/2}\text{TiO}_3\text{-BaTiO}_3)$ ceramics—I. Processing. *J. Electroceram.* **11**, 207 (2003).
15. Y. Sakka and T.S. Suzuki: Textured development of feeble magnetic ceramics by colloidal processing under high magnetic field. *J. Ceram. Soc. Jpn.* **113**, 26 (2005).
16. M.M. Seabaugh, I.H. Kerscht, and G.L. Messing: Texture development by templated grain growth in liquid phase sintered α -alumina. *J. Am. Ceram. Soc.* **80**, 1181 (1997).
17. T.S. Suzuki, T. Uchikoshi, and Y. Sakka: Control of texture in alumina by colloidal processing in a strong magnetic field. *Sci. Technol. Adv. Mater.* **7**, 356 (2006).
18. J.L. Jones, B.J. Iverson, and K.J. Bowman: Texture and anisotropy of polycrystalline piezoelectrics. *J. Am. Ceram. Soc.* **90**, 2297 (2007).
19. F.K. Lotgering: Topotactical reactions with ferrimagnetic oxides having hexagonal crystal structures-I. *J. Inorg. Nucl. Chem.* **9**, 113 (1959).
20. K.H. Brosnan, G.L. Messing, R.J. Meyer, Jr., and M.D. Vaudin: Texture measurements in (001) fiber-oriented PMN-PT. *J. Am. Ceram. Soc.* **89**, 1965 (2006).
21. W.A. Dollase: Correction for preferred orientation in powder diffractometry: Application of the March model. *J. Appl. Crystallogr.* **19**, 267 (1986).
22. L.D. Landau, L.P. Pitaevskii, and E.M. Lifshitz: *Electrodynamics of Continuous Media*, 2nd ed., Vol. **8**, Course of Theoretical Physics (Oxford University Press, Oxford, England, 2004).
23. R.C. Pullar: A review of the synthesis, properties and applications of hexaferrite ceramics. *Prog. Mater. Sci.* **57**, 1191 (2012).
24. A.L. Stuijts, G.W. Rathenau, and G.H. Weber: Ferroxdure II and III, anisotropic permanent magnet materials. In *Ferrites*, J. Smit and H.P.J. Wijn, eds., Vol. **16** (Philips Technical Library, Eindhoven, Netherlands, 1959); p. 141.
25. Y. Chen, A. Daigle, T. Fitchorov, B. Hu, M. Geiler, and A. Geiler: Electronic tuning of magnetic permeability in Co_2Z hexaferrite toward high frequency electromagnetic device miniaturization. *Appl. Phys. Lett.* **98**, 202502 (2011).
26. G. Jian, F. Meng, D. Zhou, Q. Fu, Z. Du, and C. Yan: Fabrication of textured CoFe_2O_4 ceramics by novel RTGG method using rod-like α - FeOOH particles as templates. *Mater. Chem. Phys.* **162**, 380 (2015).
27. P. Chang, L. He, D. Wei, and H. Wang: Textured z-type hexaferrite $\text{Ba}_3\text{Co}_2\text{Fe}_{24}\text{O}_{41}$, ceramics with high permeability by reactive templated grain growth method. *J. Eur. Ceram. Soc.* **36**, 2519 (2016).
28. J.P. Rush, C.J. May-Miller, K.G.B. Palmer, N.A. Rutter, A.R. Dennis, Y-H. Shi, D.A. Cardwell, and J.H. Durrell: Transport J_c in bulk superconductors: A practical approach?. *IEEE Trans. Appl. Supercond.* **26**, 6800904 (2016).
29. B. Raveau: Texturing of high- T_c superconductors. *Supercond. Sci. Technol.* **12**, R115 (1999).
30. C. His, N. Chardon, R. Kuentzler, and S. Vilminot: Elaboration and characterization of $\text{YBa}_2\text{Cu}_3\text{O}_{7-x}$ thick tapes. *J. Mater. Sci.* **26**, 4829 (1991).
31. D.M. Feldmann, T.G. Holesinger, R. Feenstra, and D.C. Larbalestier: A review of the influence of grain boundary geometry on the electromagnetic properties of polycrystalline $\text{YBa}_2\text{Cu}_3\text{O}_{7-x}$ films. *J. Am. Ceram. Soc.* **91**, 1869 (2008).
32. A. Goyal, M.P. Paranthaman, and U. Schopp: The RABiTS approach: Using rolling-assisted biaxially textured substrates for high-performance YBCO superconductors. *MRS Bull.* **29**, 552 (2004).
33. M.A. Susner, T.W. Daniels, M.D. Sumption, M.A. Rindfleisch, C.J. Thong, and E.W. Collings: Drawing induced texture and the evolution of superconductive properties with heat treatment time in powder-in-tube *in situ* processed MgB_2 strands. *Supercond. Sci. Tech.* **25**, 065002 (2012).
34. D. Dimos, P. Chaudhari, J. Mannhart, and F.K. LeGoues: Orientation dependence of grain-boundary critical currents in $\text{YBa}_2\text{Cu}_3\text{O}_{7-\delta}$ bicrystals. *Phys. Rev. Lett.* **61**, 219 (1988).
35. G-Z. Li, J-W. Li, and W-M. Yang: A combined powder melt and infiltration growth technique for fabricating nano-composited Y-Ba-Cu-O single-grain superconductor. *Supercond. Sci. Technol.* **28**, 105002 (2015).
36. Y. Shi, J.H. Durrell, A.R. Dennis, K. Huang, D.K. Namburi, D. Zhou, and D.A. Cardwell: Multiple seeding for the growth of bulk GdBCO-Ag superconductors with single grain behaviour. *Supercond. Sci. Technol.* **30**, 015003 (2017).
37. A. Bhargava, J. Schwartz, J.A. Alarco, and I.D.R. Mackinnon: Progress towards slip-casting $\text{YBa}_2\text{Cu}_3\text{O}_{7-x}$ monoliths. *Mater. Lett.* **30**, 199 (1997).
38. L.C. Pathak: Fabrication and sintering characteristics of doctor blade YBCO-Ag tapes. *Ceram. Int.* **30**, 417 (2004).
39. S.E. Dorris, M.T. Lanagan, D.M. Moffatt, H.J. Leu, C.A. Youngdahl, U. Balachandran, A. Cazzato, D.E. Bloomberg, and K.C. Goretta: Y_2BaCuO_5 as a substrate for $\text{YBa}_2\text{Cu}_3\text{O}_x$. *Jpn. J. Appl. Phys.* **28**, 1415 (1989).
40. P.J. McGinn, W. Chen, N. Zhu, U. Balachandran, and M.T. Lanagan: Texture processing of extruded $\text{YBa}_2\text{Cu}_3\text{O}_{6+x}$ wires by zone melting. *Phys. C* **165**, 480 (1990).

41. G.S. Grader and D.W. Johnson, Jr.: Forming methods for high T_c superconductors. *Thermochim. Acta* **174**, 239 (1991).
42. K.G. Frase, G.C. Farrington, and J.O. Thomas: Proton transport in the β/β'' -aluminas. *Annu. Rev. Mater. Sci.* **14**, 279 (1984).
43. J.V.L. Beckers, K.J. van der Bent, and S.W. de Leeuw: Ionic conduction in Na^+ - β -alumina studied by molecular dynamics simulation. *Solid State Ionics* **133**, 217 (2000).
44. J.W. Fergus: Ion transport in sodium ion conducting solid electrolytes. *Solid State Ionics* **227**, 102 (2012).
45. L.C. de Jonghe and J.B. Hall: Ion current concentration in grain boundaries of sodium beta alumina. *Scr. Mater.* **10**, 285 (1976).
46. L.C. De Jonghe: Grain boundaries and ionic conduction in sodium beta alumina. *J. Mater. Sci.* **14**, 33 (1979).
47. C.K. Kuo, A. Tan, and P.S. Nicholson: Solid state ionics impedance analysis as a tool for designing β'' -alumina microstructures. *Solid State Ionics* **48**, 315 (1991).
48. A. Kishimoto and K. Shimokawa: Preferential orientation dependent mechanical and electrical properties in $\text{Na}\beta$ -alumina ceramics. *Key Eng. Mater.* **301**, 147 (2006).
49. A. Hooper: A study of the electrical properties of single-crystal and polycrystalline β -alumina using complex plane analysis. *J. Phys. D: Appl. Phys.* **10**, 1487 (1977).
50. A. Tan, C.K. Kuo, and P.S. Nicholson: Preparation and characterization of textured polycrystalline Na and K- β -aluminas. *Solid State Ionics* **42**, 233 (1990).
51. A. Tan, C. Kun Kuo, and P.S. Nicholson: The influence of grain boundaries on the conductivity and ion-exchange rate of β'' -alumina polycrystalline isomorphs. *Solid State Ionics* **45**, 137 (1991).
52. T. Ohta, M. Harata, and A. Imai: Preferred orientation on beta-alumina ceramics. *Mater. Res. Bull.* **11**, 1343 (1976).
53. A.V. Virkar, G.R. Miller, and R.S. Gordon: Resistivity-microstructure relations in lithia-stabilized polycrystalline β'' -alumina. *J. Am. Ceram. Soc.* **61**, 250 (1978).
54. E. Butcherit, J. Schoonman, H.W. Zandbergen, C. Lutz-Elsner, M. Schreiber, and P. Wang: Microstructure-conductivity relationships in solid anisotropic ionically conducting materials. *Mater. Res. Soc. Symp. Proc.* **369**, 433 (1995).
55. A.P. De Kroon, F. Gstrein, G.W. Schafer, and F. Aldinger: Ionic conductivity of dense K- β -alumina ceramics: Microstructural dependence and the influence of phase transformations. *Solid State Ionics* **133**, 107 (2000).
56. H. Asaoka, R. Ogawa, H. Hayashi, and A. Kishimoto: Influence of kinds of aluminum source on the preferential orientation and properties of $\text{Na}\beta$ -alumina ceramics. *J. Ceram. Soc. Jpn.* **114**, 719 (2006).
57. J.L. Shi, J.H. Gao, and Z.X. Lin: The relation between microstructure and ionic conductivity of hot-pressed β - Al_2O_3 . *J. Mater. Sci.* **24**, 1827 (1989).
58. K. Koganei, T. Oyama, M. Inada, N. Enomoto, and K. Hayashi: C-axis oriented β'' -alumina ceramics with anisotropic ionic conductivity prepared by spark plasma sintering. *Solid State Ionics* **267**, 22 (2014).
59. R. Subasri and H. Näfe: Texture in $\text{Na}\beta$ - Al_2O_3 due to microwave processing. *Mater. Chem. Phys.* **112**, 16 (2008).
60. Y. Sakka, A. Honda, T.S. Suzuki, and Y. Moriyoshi: Fabrication of oriented β -alumina from porous bodies by slip casting in a high magnetic field. *Solid State Ionics* **172**, 341 (2004).
61. Y. Sakka, T.S. Suzuki, and T. Uchikoshi: Fabrication and some properties of textured alumina-related compounds by colloidal processing in high-magnetic field and sintering. *J. Eur. Ceram. Soc.* **28**, 935 (2008).
62. V.V. Kharton, F.M.B. Marques, and A. Atkinson: Transport properties of solid oxide electrolyte ceramics: A brief review. *Solid State Ionics* **174**, 135 (2004).
63. K.R. Kendall, C. Navas, J.K. Thomas, and H-C. Zur Loye: Recent developments in oxide ion conductors: Aurivillius phases. *Chem. Mater.* **8**, 642 (1996).
64. N. Mahato, A. Banerjee, A. Gupta, S. Omar, and K. Balani: Progress in material selection for solid state oxide fuel cell technology: A review. *Prog. Mater. Sci.* **72**, 141 (2015).
65. L. Malavasi, C.A.J. Fisher, and M.S. Islam: Oxide-ion and proton conducting electrolyte materials for clean energy applications: Structural and mechanistic features. *Chem. Soc. Rev.* **39**, 4370 (2010).
66. K. Fukuda, T. Asaka, S. Hara, M. Oyabu, A. Berghout, E. Béchade, O. Masson, I. Julien, and P. Thomas: Crystal structure and oxide-ion conductivity along c -axis of Si-deficient apatite-type lanthanum silicate. *Chem. Mater.* **25**, 2154 (2013).
67. K. Fukuda, M. Okabe, and T. Asaka: Microtexture of c -axis-oriented polycrystalline lanthanum silicate oxyapatite formed by reactive diffusion. *J. Am. Ceram. Soc.* **99**, 2816 (2016).
68. D.L. Medlin and G.J. Snyder: Interfaces in bulk thermoelectric materials: A review for current opinion in colloid and interface science. *Curr. Opin. Colloid Interface Sci.* **14**, 226 (2009).
69. H. Ohta, W-S. Seo, and K. Koumoto: Thermoelectric properties of homologous compounds in the $\text{ZnO-In}_2\text{O}_3$ system. *J. Am. Ceram. Soc.* **79**, 2193 (1996).
70. I. Terasaki, Y. Sasago, and K. Uchinokura: Large thermoelectric power in NaCo_2O_4 single crystals. *Phys. Rev. B: Condens. Matter Mater. Phys.* **56**, R12685 (1997).
71. S. Li, R. Funahashi, I. Matsubara, K. Ueno, and H. Yamada: High temperature thermoelectric properties of oxide $\text{Ca}_9\text{Co}_{12}\text{O}_{28}$. *J. Mater. Chem.* **9**, 1659 (1999).
72. J. Hejtmánek, M. Veverka, K. Knížek, H. Fujishiro, S. Hebert, Y. Klein, A. Maignan, C. Bellouard, and B. Lenoir: *Cobaltites as Perspective Thermoelectrics*, edited by J. Yang (Mater. Res. Soc. Symp. Proc. **886**, Warrendale, PA, 2006) 1274-F01-07.1.
73. H. Itahara, S. Tajima, and T. Tani: Synthesis of β - $\text{Co}(\text{OH})_2$ platelets by precipitation and hydrothermal methods. *J. Ceram. Soc. Jpn.* **110**, 1048 (2002).
74. K. Koumoto, R. Funahashi, E. Guilmeau, Y. Miyazaki, A. Weidenkaff, Y. Wang, and C. Wan: Thermoelectric ceramics for energy harvesting. *J. Am. Ceram. Soc.* **96**(1), 1 (2013).
75. Y. Zhou, I. Matsubara, S. Horii, T. Takeuchi, R. Funahashi, M. Shikano, J. Shimoyama, K. Kishio, W. Shin, N. Izu, and N. Murayama: Thermoelectric properties of highly grain-aligned and densified Co-based oxide ceramics. *J. Appl. Phys.* **93**, 2653 (2003).
76. R. Funahashi, S. Urata, T. Sano, and M. Kitawaki: Enhancement of thermoelectric figure of merit by incorporation of large single crystals in $\text{Ca}_3\text{Co}_4\text{O}_9$ bulk materials. *J. Mater. Res.* **18**, 1646 (2003).
77. M. Prevel, E.S. Reddy, O. Perez, W. Kobayashi, I. Terasaki, C. Goupil, and J.G. Noudem: Thermoelectric properties of sintered and textured Nd-Substituted $\text{Ca}_3\text{Co}_4\text{O}_9$ ceramics. *JJAP* **46**, 97 (2007).
78. M. Prevel, S. Lemonnier, Y. Klein, S. Hebert, D. Chateigner, B. Ouladdiaf, and J.G. Noudem: Textured $\text{Ca}_3\text{Co}_4\text{O}_9$ thermoelectric oxides by thermoforging process. *J. Appl. Phys.* **98**, 093706 (2005).
79. E. Guilmeau, R. Funahashi, M. Mikami, K. Chong, and D. Chateigner: Thermoelectric properties-texture relationship in highly oriented $\text{Ca}_3\text{Co}_4\text{O}_9$ composited. *Appl. Phys. Lett.* **85**, 1490 (2004).
80. Y.H. Liu, Y.H. Lin, Z. Shi, C.W. Nan, and Z.J. Shen: Preparation of $\text{Ca}_3\text{Co}_4\text{O}_9$ and improvement of its thermoelectric properties by spark plasma sintering. *J. Am. Ceram. Soc.* **88**, 1337 (2005).
81. H.Q. Liu, Y. Song, S.N. Zhang, X.B. Zhao, and F.R. Wang: Thermoelectric properties of $\text{Ca}_{3-x}\text{Y}_x\text{Co}_4\text{O}_{9+\delta}$ ceramics. *J. Phys. Chem. Solids* **70**, 600 (2009).

82. J.G. Noudem, D. Kenfaui, D. Chateigner, and M. Gomina: Granular and lamellar thermoelectric oxides consolidated by spark plasma sintering. *J. Electron. Mater.* **40**, 1100 (2011).
83. H. Itahara, J. Sugiyama, and T. Tani: Enhancement of electrical conductivity in thermoelectric $[\text{Ca}_2\text{CoO}_3]_{0.62}[\text{CoO}_2]$ ceramics by texture improvement. *Jpn. J. Appl. Phys.* **43**, 5134 (2004).
84. S. Lee, R.H.T. Wilke, S. Trolier-McKinstry, S. Zhang, and C.A. Randall: $\text{Sr}_x\text{Ba}_{1-x}\text{Nb}_2\text{O}_{6-\delta}$ ferroelectric-thermoelectrics: Crystal anisotropy, conduction mechanism, and power factor. *Appl. Phys. Lett.* **96**, 031910 (2010).
85. S. Lee, S. Dursun, C. Duran, and C.A. Randall: Thermoelectric power factor enhancement of textured ferroelectric $\text{Sr}_x\text{Ba}_{1-x}\text{Nb}_2\text{O}_{6-\delta}$. *J. Mater. Res.* **26**(1), 26 (2011).
86. Y. Miwa, S. Kawada, M. Kimura, S. Omiya, N. Kubodera, A. Ando, T.S. Suzuki, T. Uchikoshi, and Y. Sakka: Processing and enhanced piezoelectric properties of highly oriented compositionally modified $\text{Pb}(\text{Zr},\text{Ti})\text{O}_3$ ceramics fabricated by magnetic alignment. *Appl. Phys. Express* **8**, 041501 (2015).
87. E.M. Sabolsky, S. Trolier-McKinstry, and G.L. Messing: Dielectric and piezoelectric properties of (001) fiber-textured $0.675\text{Pb}(\text{Mg}_{1/3}\text{Nb}_{2/3})\text{O}_3-0.325\text{PbTiO}_3$ ceramics. *J. Appl. Phys.* **93**, 4072 (2003).
88. T. Richter, S. Denneler, C. Schuh, E. Suvaci, and R. Moos: Textured PMN-PT and PMN-PZT. *J. Am. Ceram. Soc.* **91**, 929 (2008).
89. Y. Yan, Y.U. Wang, and S. Priya: Electromechanical behavior of [001]-textured $\text{Pb}(\text{Mg}_{1/3}\text{Nb}_{2/3})\text{O}_3-\text{PbTiO}_3$ ceramics. *Appl. Phys. Lett.* **100**, 192950 (2012).
90. K.H. Brosnan: Processing, properties, and application of textured $0.72\text{Pb}(\text{Mg}_{1/3}\text{Nb}_{2/3})\text{O}_3-0.28\text{PbTiO}_3$ ceramics. Ph.D thesis, Pennsylvania State University, 2007.
91. H. Amorin, H. Ursic, P. Ramos, J. Holc, R. Moreno, D. Chateigner, J. Ricote, and M. Alguero: $\text{Pb}(\text{Mg}_{1/3}\text{Nb}_{2/3})\text{O}_3-\text{PbTiO}_3$ textured ceramics with high piezoelectric response by a novel templated grain growth approach. *J. Am. Ceram. Soc.* **97**, 420 (2014).
92. S.F. Poterala, S. Trolier-McKinstry, R.J. Meyer, Jr., and G.L. Messing: Processing, texture quality, and piezoelectric properties of (001)_C textured $(1-x)\text{Pb}(\text{Mg}_{1/3}\text{Nb}_{2/3})\text{TiO}_3-x\text{PbTiO}_3$ ceramics. *J. Appl. Phys.* **110**, 14105 (2011).
93. Y. Yan, L. Yang, Y. Zhou, K.H. Cho, J.S. Heo, and S. Priya: Enhanced temperature stability in (111) textured tetragonal $\text{Pb}(\text{Mg}_{1/3}\text{Nb}_{2/3})\text{O}_3-\text{PbTiO}_3$ piezoelectric ceramics. *J. Appl. Phys.* **118**, 104101 (2015).
94. Y. Yan, J.E. Zhou, D. Maurya, Y.U. Wang, and S. Priya: Giant piezoelectric voltage coefficient in grain-oriented modified PbTiO_3 material. *Nat. Commun.* **7**, 1 (2016).
95. Y. Chang, J. Wu, Y. Sun, S. Zhang, X. Wang, B. Yang, G.L. Messing, and W. Cao: Enhanced electromechanical properties and phase transition temperatures in [001] textured $\text{Pb}(\text{In}_{1/2}\text{Nb}_{1/2})\text{O}_3-\text{Pb}(\text{Mg}_{1/3}\text{Nb}_{2/3})\text{O}_3-\text{PbTiO}_3$ ternary ceramics. *Appl. Phys. Lett.* **107**, 82902 (2015).
96. D. Wei, Q. Yuan, G. Zhang, and H. Wang: Templated grain growth and piezoelectric properties of (001)-textured PIN-PMN-PT ceramics. *J. Mater. Res.* **30**, 2144 (2015).
97. C. Duran, S. Dursun, and E. Akça: High strain, (001)-textured $\text{Pb}(\text{Mg}_{1/3}\text{Nb}_{2/3})\text{O}_3-\text{Pb}(\text{Yb}_{1/2}\text{Nb}_{1/2})\text{O}_3-\text{PbTiO}_3$ piezoelectric ceramics. *Scr. Mater.* **113**, 14 (2016).
98. Y. Yan, K. Cho, D. Maurya, A. Kumar, S. Kalinin, K. Armen, and S. Priya: Giant energy density in [001]-textured $\text{Pb}(\text{Mg}_{1/3}\text{Nb}_{2/3})\text{O}_3-\text{PbZrO}_3-\text{PbTiO}_3$ piezoelectric ceramics. *Appl. Phys. Lett.* **102**, 42903 (2013).
99. Y. Yan and S. Priya: Strong piezoelectric anisotropy d_{15}/d_{33} in (111) textured $\text{Pb}(\text{Mg}_{1/3}\text{Nb}_{2/3})\text{O}_3-\text{Pb}(\text{Zr},\text{Ti})\text{O}_3$ ceramics. *Appl. Phys. Lett.* **107**, 82909 (2015).
100. S.J. Zhang, J. Luo, W. Hackenberger, N.P. Sherlock, R.J. Meyer, Jr., and T.R. Shrout: Electromechanical characterization of $\text{Pb}(\text{In}_{1/2}\text{Nb}_{1/2})\text{O}_3-\text{Pb}(\text{Mg}_{1/3}\text{Nb}_{2/3})-\text{PbTiO}_3$ crystals as a function of crystallographic orientation and temperature. *J. Appl. Phys.* **105**, 104506 (2009).
101. Y. Saito, H. Takao, T. Tani, T. Nonoyama, K. Takatori, T. Homma, T. Nagaya, and M. Nakamura: Lead-free piezoceramics. *Nature* **432**, 84 (2004).
102. Z.P. Yang, Y.F. Chang, and L.L. Wei: Phase transitional behavior and electrical properties of lead-free $(\text{K}_{0.44}\text{Na}_{0.52}\text{Li}_{0.04})(\text{Nb}_{0.96-x}\text{Ta}_x\text{Sb}_{0.04})\text{O}_3$ piezoelectric ceramics. *Appl. Phys. Lett.* **90**, 042911 (2007).
103. J.G. Wu and D.Q. Xiao: Compositional dependence of phase structure and electrical properties in $(\text{K}_{0.42}\text{Na}_{0.58})\text{NbO}_3-\text{LiSbO}_3$ lead-free ceramics. *J. Appl. Phys.* **102**, 114113 (2007).
104. J. Fuentes, J. Portelles, M.D. Durruthy-Rodriguez, H. H'Mok, O. Raymond, J. Heiras, M.P. Cruz, and J.M. Siqueiros: Dielectric and piezoelectric properties of the KNN ceramic compound doped with Li, La and Sb. *Appl. Phys. A* **117**, 709 (2015).
105. Y.B. Wei, Z. Wu, Y.M. Jia, J. Wu, Y.C. Shen, and H.S. Luo: Dual-enhancement of ferro-/piezoelectric and photoluminescent performance in Pr^{3+} doped $(\text{K}_{0.5}\text{Na}_{0.5})\text{NbO}_3$ lead-free ceramics. *Appl. Phys. Lett.* **105**, 042902 (2014).
106. Y. Chang, S.F. Poterala, Z. Yang, S. Trolier-McKinstry, and G.L. Messing: (001) textured $(\text{K}_{0.5}\text{Na}_{0.5})(\text{Nb}_{0.97}\text{Sb}_{0.03})\text{O}_3$ piezoelectric ceramics with high electromechanical coupling over a broad temperature range. *Appl. Phys. Lett.* **95**, 232905 (2009).
107. Y. Chang, S. Poterala, Z. Yang, and G.L. Messing: Enhanced electromechanical properties and temperature stability of textured $(\text{K}_{0.5}\text{Na}_{0.5})\text{NbO}_3$ -based piezoelectric ceramics. *J. Am. Ceram. Soc.* **94**, 2494 (2011).
108. H. Takao, Y. Saito, Y. Aoki, and K. Horibuchi: Microstructural evolution of crystalline-oriented $(\text{K}_{0.5}\text{Na}_{0.5})\text{NbO}_3$ piezoelectric ceramics with a pintering aid of CuO. *J. Am. Ceram. Soc.* **89**, 1951 (2006).
109. A. Hussain, J.S. Kim, T.K. Song, M.H. Kim, W.J. Kim, and S.S. Kim: Fabrication of textured KNNT ceramics by reactive template grain growth using NN templates. *Curr. Appl. Phys.* **13**, 1055 (2013).
110. Y. Saito and H. Takao: Synthesis of polycrystalline platelike KNbO_3 particles by the topochemical micro-crystal conversion method and fabrication of grain-oriented $(\text{K}_{0.5}\text{Na}_{0.5})\text{NbO}_3$ ceramics. *J. Eur. Ceram. Soc.* **27**, 4085 (2007).
111. A.B. Haugen, G. Henning, F. Madaro, M.I. Morozov, G. Tutuncu, J.L. Jones, T. Grande, and M. Einarsrud: Piezoelectric $\text{K}_{0.5}\text{Na}_{0.5}\text{NbO}_3$ ceramics textured using needlelike $\text{K}_{0.5}\text{Na}_{0.5}\text{NbO}_3$ templates. *J. Am. Ceram. Soc.* **97**, 3818 (2014).
112. Y. Li, C. Hui, M. Wu, Y. Li, and Y. Wang: Textured $(\text{K}_{0.5}\text{Na}_{0.5})\text{NbO}_3$ ceramics prepared by screen-printing multilayer grain growth technique. *Ceram. Int.* **38S**, S283 (2012).
113. G. Tutuncu, Y. Chang, S. Poterala, J.L. Jones, and G.L. Messing: *In situ* observations of template grain growth in $(\text{Na}_{0.5}\text{K}_{0.5})_{0.98}\text{Li}_{0.02}\text{NbO}_3$ piezoceramics: Texture development and template-matrix interactions. *J. Am. Ceram. Soc.* **95**, 2653 (2012).
114. F. Gao, R.Z. Hong, J.J. Li, Y.H. Yao, and C.S. Tian: Effect of different templates on microstructure of textured $\text{Na}_{0.5}\text{Bi}_{0.5}\text{TiO}_3-\text{BaTiO}_3$ ceramics with RTGG method. *J. Eur. Ceram. Soc.* **28**, 2063 (2008).
115. W. Bai, J. Hao, F. Fu, W. Li, B. Shen, and J. Zhai: Structure and strain behavior of (001) textured BNT-based ceramics by template grain growth. *Mater. Lett.* **97**, 137 (2013).
116. M. Deng, X. Li, Z. Zhao, T. Li, Y. Dai, and H. Ji: Crystallographic textured evolution in $0.85\text{Na}_{0.5}\text{Bi}_{0.5}\text{TiO}_3-0.04\text{BaTiO}_3-0.11\text{K}_{0.5}\text{Bi}_{0.5}\text{TiO}_3$ ceramics prepared by reactive-templated grain growth method. *J. Mater. Sci. Mater. Electron.* **25**, 1873 (2014).

117. F. Gao, X. Liu, C. Zhang, L. Cheng, and C. Tian: Fabrication and electrical properties of textured $(\text{Na,K})_{0.5}\text{Bi}_{0.5}\text{TiO}_3$ ceramics by reactive-templated grain growth. *Ceram. Int.* **34**, 403 (2008).
118. D. Hu, K. Mori, X. Kong, K. Shinagawa, S. Wada, and Q. Feng: Fabrication of [100]-oriented bismuth sodium titanate ceramics with small grain size and high density for piezoelectric materials. *J. Eur. Ceram. Soc.* **34**, 1169 (2014).
119. H. Zou, Y. Sui, X. Zhu, B. Liu, J. Xue, and J. Zhang: Texture development and enhanced electromechanical properties in $\langle 001 \rangle$ -textured BNT-based materials. *Mater. Lett.* **184**, 139 (2016).
120. T. Shoji, Y. Yoshida, and T. Kimura: Mechanism of texture development in $\text{Bi}_{0.5}(\text{Na,K})_{0.5}\text{TiO}_3$ templated by platelike Al_2O_3 particles. *J. Am. Ceram. Soc.* **91**, 3883 (2008).
121. T. Shoji, K. Fuse, and T. Kimura: Mechanism of texture development in $\text{Bi}_{0.5}(\text{Na,K})_{0.5}\text{TiO}_3$ prepared by the templated grain growth process. *J. Am. Ceram. Soc.* **92**, S140 (2009).
122. X. Jing, Y. Li, Q. Yang, J. Zeng, and Q. Yin: Influence of different templates on the textured $\text{Bi}_{0.5}(\text{Na}_{1-x}\text{K}_x)_{0.5}\text{TiO}_3$ piezoelectric ceramics by the reactive templated grain growth process. *Ceram. Int.* **30**, 1889 (2004).
123. D. Maurya, Y. Zhou, Y. Yan, and S. Priya: Synthesis mechanism of grain-oriented lead-free piezoelectric $\text{Na}_{0.5}\text{Bi}_{0.5}\text{TiO}_3$ - BaTiO_3 ceramics with giant piezoelectric response. *J. Mater. Chem. C* **1**, 2102 (2013).
124. D. Maurya, Y. Zhou, Y. Wang, Y.K. Yan, J.F. Li, D. Viehland, and S. Priya: Giant strain with ultra-low hysteresis and high temperature stability in grain oriented lead-free $\text{K}_{0.5}\text{Bi}_{0.5}\text{TiO}_3$ - BaTiO_3 - $\text{Na}_{0.5}\text{Bi}_{0.5}\text{TiO}_3$ piezoelectric materials. *Sci. Rep.* **5**, 8595 (2014).
125. H. Zhang, P. Xu, E. Patterson, J. Zang, S. Jiang, and J. Rödel: Preparation and enhanced electrical properties of grain-oriented $(\text{Bi}_{1/2}\text{Na}_{1/2})\text{TiO}_3$ -based lead-free incipient piezoceramics. *J. Eur. Ceram. Soc.* **35**, 2501 (2015).
126. S. Ma, Y. Zhang, Z. Liu, X. Dai, and J. Huang: Preparation and enhanced electric-field-induced strain of textured 91BNT-6BT-3KNN lead-free piezoceramics by TGG method. *J. Mater. Sci. Mater. Electron.* **27**, 3076 (2016).
127. D. Vriami, D. Damjanovic, J. Vleugels, and O. Van Der Biest: Textured BaTiO_3 by templated grain growth and electrophoretic deposition. *J. Mater. Sci.* **50**, 7896 (2015).
128. F. Fu, B. Shen, Z. Xu, and J. Zhai: Electric properties of BaTiO_3 lead-free textured piezoelectric thick film by screen printing method. *J. Electroceram.* **33**, 208 (2014).
129. S. Wada, K. Takeda, T. Muraishi, H. Kakemoto, T. Tsurumi, and T. Kimura: Preparation of [110] grain oriented barium titanate ceramics by templated grain growth method and their piezoelectric properties. *Jpn. J. Appl. Phys.* **46**, 739 (2007).
130. A.N. Kamlo, P.M. Geffroy, M. Pham-Thi, and P. Marchet: {111}-Textured BaTiO_3 ceramics elaborated by templated grain growth using NaNbO_3 templates. *Mater. Lett.* **113**, 149 (2013).
131. W. Liu and X. Ren: Large piezoelectric effect in Pb-free ceramics. *Phys. Rev. Lett.* **103**, 257602 (2009).
132. T. Sato and T. Kimura: Preparation of $\langle 111 \rangle$ textured BaTiO_3 ceramics by templated grain growth method using novel template particles. *Ceram. Int.* **34**, 757 (2008).
133. S.K. Ye, J.Y.H. Fuh, and L. Lu: Structure and electrical properties of $\langle 001 \rangle$ textured $(\text{Ba}_{0.85}\text{Ca}_{0.15})(\text{Ti}_{0.9}\text{Zr}_{0.1})\text{O}_3$ lead-free piezoelectric ceramics. *Appl. Phys. Lett.* **100**, 252906 (2012).
134. E.M. Sabolsky, L. Maldonado, M.M. Seabaugh, and S.L. Swartz: Textured- $\text{Ba}(\text{Zr,Ti})\text{O}_3$ piezoelectric ceramics fabricated by templated grain growth (TGG). *J. Electroceram.* **25**, 77 (2010).
135. W. Bai, D. Chen, P. Li, B. Shen, J. Zhai, and Z. Ji: Enhanced electromechanical properties in $\langle 001 \rangle$ -textured $(\text{Ba}_{0.85}\text{Ca}_{0.15})(\text{Zr}_{0.1}\text{Ti}_{0.9})\text{O}_3$ lead-free piezoceramics. *Ceram. Int.* **42**, 3429 (2016).
136. S. Zhukov, Y.A. Genenko, J. Koruza, J. Schultheiß, H.v. Seggern, W. Sakamoto, H. Ichikawa, T. Murata, K. Hayashi, and T. Yogo: Effect of texturing on polarization switching dynamics in ferroelectric ceramics. *Appl. Phys. Lett.* **108**, 012907 (2016).
137. J. Schultheiß, O. Clemens, S. Zhukov, H.v. Seggern, W. Sakamoto, and J. Koruza: Effect of degree of crystallographic texture on ferro- and piezoelectric properties of $\text{Ba}_{0.85}\text{Ca}_{0.15}\text{TiO}_3$ piezoceramics. *J. Am. Ceram. Soc.* (2017). doi: 10.1111/jace.14749.
138. S. Ye, J. Fuh, L. Lu, Y-I. Chang, and J-R. Yang: Structure and properties of hot-pressed lead-free $(\text{Ba}_{0.85}\text{Ca}_{0.15})(\text{Zr}_{0.1}\text{Ti}_{0.9})\text{O}_3$ piezoelectric ceramics. *RSC Adv.* **3**, 20693 (2013).
139. S. Endo, H. Nagata, and T. Takenaka: Fabrication and high power piezoelectric characteristics of textured $(\text{Sr}_{0.7}\text{Ca}_{0.3})_2\text{Bi}_4\text{Ti}_5\text{O}_{18}$. *Jpn. J. Appl. Phys.* **53**, 3 (2014).
140. H. Zhang, H. Yan, X. Zhang, M.J. Reece, J. Liu, Z. Shen, Y. Kan, and P. Wang: The effect of texture on the properties of $\text{Bi}_{3.15}\text{Nd}_{0.85}\text{Ti}_3\text{O}_{12}$ ceramics prepared by spark plasma sintering. *Mater. Sci. Eng., A* **475**, 92 (2008).
141. T. Kimura, Y. Sakuma, and M. Murata: Texture development in piezoelectric ceramics by templated grain growth using hetero-templates. *J. Eur. Ceram. Soc.* **25**, 2227 (2005).
142. M. Kimura, H. Ogawa, T. Sawada, K. Shiratsuyu, N. Wada, and A. Ando: Piezoelectric properties in textured ceramics of bismuth layer-structured ferroelectrics. *J. Electroceram.* **21**, 55 (2008).
143. H. Chen, B. Shen, J. Xu, and J. Zhai: Textured $\text{Ca}_{0.85}(\text{Li,Ce})_{0.15}\text{Bi}_4\text{Ti}_4\text{O}_{15}$ ceramics for high temperature piezoelectric applications. *Mater. Res. Bull.* **47**, 2530 (2012).
144. H. Chen and J. Zhai: Enhanced piezoelectric properties of $\text{CaBi}_2\text{Nb}_2\text{O}_9$ with Eu modification and templated grain growth. *Key Eng. Mater.* **515**, 1367 (2012).
145. H. Hao, H. Liu, and S. Ouyang: Processing and property of textured lead-free $\text{SrTi}_4\text{Bi}_4\text{O}_{15}$ piezoelectric ceramics. *J. Electroceram.* **21**, 255 (2008).
146. T. Li, X. Li, Z. Zhao, H. Ji, and Y. Dai: Structures and electrical properties of textured $\text{Ca}_{0.85}(\text{Li,Ce})_{0.075}\text{Bi}_4\text{Ti}_4\text{O}_{15}$ ceramics prepared by the reactive templated grain growth. *Integr. Ferroelectr.* **162**, 1 (2015).
147. J. Liu, Z. Shen, M. Nygren, Y. Kan, and P. Wang: SPS processing of bismuth-layer structured ferroelectric ceramics yielding highly textured microstructures. *J. Eur. Ceram. Soc.* **26**, 3233 (2006).
148. Q.X. Bao, L.H. Zhu, Q.W. Huang, and J. Xv: Preparation of textured $\text{Ba}_2\text{NaNb}_5\text{O}_{15}$ ceramics by templated grain growth. *Ceram. Int.* **32**(7), 745 (2006).
149. S. Dursun, E. Mensur-Alkoy, and S. Alkoy: Fabrication of textured lead-free strontium barium niobate (SBN61) bulk ceramics and their electrical properties. *J. Eur. Ceram. Soc.* **36**, 2479 (2016).
150. Y. Chang, S. Lee, S. Poterala, C.A. Randall, and G.L. Messing: A critical evaluation of reactive templated grain growth (RTGG) mechanisms in highly [001] textured $\text{Sr}_{0.61}\text{Ba}_{0.39}\text{Nb}_2\text{O}_6$ ferroelectric-thermoelectrics. *J. Mater. Res.* **26**(24), 3044 (2011).
151. L. Wei, X. Chao, X. Han, and Z. Yang: Structure and electrical properties of textured $\text{Sr}_{1.85}\text{Ca}_{0.15}\text{NaNb}_5\text{O}_{15}$ ceramics prepared by reactive templated grain growth. *Mater. Res. Bull.* **52**, 65 (2014).
152. L. Liu and Z. Hou: Fabrication of grain-oriented $\text{KSr}_2\text{Nb}_5\text{O}_{15}$ ceramics by a brush technique. *Mater. Lett.* **186**, 105 (2017).
153. S. Alkoy and S. Dursun: Processing and properties of textured potassium strontium niobate ($\text{KSr}_2\text{Nb}_5\text{O}_{15}$) ceramic fibers—Texture development. *J. Am. Ceram. Soc.* **95**(3), 937 (2012).
154. S. Alkoy and S. Dursun: Processing and properties of textured potassium strontium niobate ($\text{KSr}_2\text{Nb}_5\text{O}_{15}$) ceramic fibers-effect

- of texture on the electrical properties. *IEEE Trans. Ultrason., Ferroelectr., Freq. Control* **60**, 2044 (2013).
155. S. Tanaka, T. Takahashi, and R. Furushima: Fabrication of c-axis-oriented potassium strontium niobate ($\text{KSr}_2\text{Nb}_5\text{O}_{15}$) ceramics by a rotating magnetic field and electrical property. *J. Ceram. Soc. Japan* **118**, 722 (2010).
156. R. Apetz and M.P.B. van Bruggen: Transparent alumina: A light-scattering model. *J. Am. Ceram. Soc.* **86**, 480 (2003).
157. P. Liu, H. Yi, G. Zhou, J. Zhang, and S. Wang: HIP and pressureless sintering of transparent alumina shaped by magnetic field assisted slip casting. *Opt. Mater. Exp.* **5**, 441 (2015).
158. A. Pringuet, T. Takahashi, S. Baba, Y. Kamo, Z. Kato, K. Uematsu, and S. Tanaka: Fabrication of transparent grain-oriented polycrystalline alumina by colloidal processing. *J. Am. Ceram. Soc.* **99**, 3217 (2016).
159. S. Tanaka, T. Takahashi, and K. Uematsu: Fabrication of transparent crystal-oriented polycrystalline strontium barium niobate ceramics for electro-optical application. *J. Eur. Ceram. Soc.* **34**, 3723 (2014).
160. J. Akiyama, Y. Sato, and T. Taira: Laser demonstration of diode-pumped Nd^{3+} -doped fluorapatite anisotropic ceramics. *Appl. Phys. Exp.* **4**, 002703 (2011).
161. Y. Sato, J. Akiyama, and T. Taira: Micro-domain controlled anisotropic laser ceramics assisted by rare-earth trivalent, in *Pacific Rim Laser Damage 2011: Optical Materials for High Power Lasers*, edited by J. Shao, K. Sugioka, and C.J. Stolz (Proc. of SPIE **8206**, Bellingham, WA, 2012) p. 82061T-1.
162. Y. Sato, M. Arzakantsyan, J. Akiyama, and T. Taira: Anisotropic Yb:FAP laser ceramics by micro-domain control. *Opt. Mater. Exp.* **4**, 214969 (2006).
163. I. Shoji, Y. Sato, S. Kurimura, V. Lupei, T. Taira, A. Ikesue, and K. Yoshida: Thermal-birefringence-induced depolarization in Nd:YAG ceramics. *Opt. Lett.* **27**, 234 (2002).
164. I. Shoji and T. Taira: Intrinsic reduction of the depolarization loss in solid-state lasers by use of a (110)-cut $\text{Y}_3\text{Al}_5\text{O}_{12}$ crystal. *Appl. Phys. Lett.* **80**, 3048 (2002).
165. S. Arakawa, H. Kadoura, T. Uyama, K. Takatori, Y. Takeda, and T. Tani: Formation of preferentially oriented $\text{Y}_3\text{Al}_5\text{O}_{12}$ film on a reactive sapphire substrate: Phase and texture transitions from Y_2O_3 . *J. Eur. Ceram. Soc.* **36**, 663 (2016).
166. K. Watari: High thermal conductivity non-oxide ceramics. *J. Ceram. Soc. Jpn.* **109**, S7 (2001).
167. N. Hirosaki, S. Ogata, C. Kocer, H. Kitagawa, and Y. Nakamura: Molecular dynamics calculation of the ideal thermal conductivity of single-crystal. *Phys. Rev. B: Condens. Matter Mater. Phys.* **65**, 134110 (2002).
168. T.S. Suzuki and Y. Sakka: Preparation of oriented bulk 5 wt% Y_2O_3 -AlN ceramics by slip casting in a high magnetic field and sintering. *Scr. Mater.* **52**, 583 (2005).
169. T.S. Suzuki, T. Uchikoshi, and Y. Sakka: Effect of sintering additive on crystallographic orientation in AlN prepared by slip casting in a strong magnetic field. *J. Eur. Ceram. Soc.* **29**, 2627 (2009).
170. B. Li, L. Pottier, J.P. Roger, D. Fournier, K. Watari, and K. Hirao: Measuring the anisotropic thermal diffusivity of silicon nitride grains by thermoreflectance microscopy. *J. Eur. Ceram. Soc.* **19**, 1631 (1999).
171. X. Zhu, T.S. Suzuki, T. Uchikoshi, and Y. Sakka: Texturing behavior in sintered reaction-bonded silicon nitride via strong magnetic field alignment. *J. Eur. Ceram. Soc.* **28**, 929 (2008).
172. X.W. Zhu, Y. Sakka, Y. Zhou, K. Hirao, and K. Itatani: A strategy for fabricating textured silicon nitride with enhanced thermal conductivity. *J. Eur. Ceram. Soc.* **34**, 2585 (2014).
173. K. Hirao, K. Watari, M.E. Brito, M. Toriyama, and S. Kanzaki: High thermal conductivity in silicon nitride with anisotropic microstructure. *J. Am. Ceram. Soc.* **79**, 2485 (1996).
174. Y. Akimune, F. Munakata, K. Matsuo, N. Hirosaki, Y. Okamoto, and K. Misono: Raman spectroscopy analysis of structural defects in hot isostatically pressed silicon nitride. *J. Ceram. Soc. Jpn.* **107**, 339 (1999).
175. McColm: *Ceramic Hardness*, 1st ed. (Plenum Press, New York, 1990).
176. T. Carisey, I. Levin, and D.G. Brandon: Microstructure and mechanical properties of textured Al_2O_3 . *J. Eur. Ceram. Soc.* **15**, 283 (1995).
177. S. Lee, Y. Lee, Y. Kim, R. Xie, M. Mitomo, and G. Zhan: Mechanical properties of hot-forged silicon carbide ceramics. *Scr. Mater.* **52**, 153 (2005).
178. V.R. Vedula, S.J. Glass, D.M. Saylor, G.S. Rohrer, W.C. Carter, S.A. Langer, and E.R. Fuller, Jr.: Residual stress predictions in polycrystalline alumina. *J. Am. Ceram. Soc.* **84**, 2947 (2001).
179. J.A. Salem, J.L. Shannon, and R.C. Bradt: The effect of texture on the crack growth resistance of alumina. Presented at the *89th Annual Meeting of the American Ceramic Society* (1987). Available at: <https://ntrs.nasa.gov/archive/nasa/casi.ntrs.nasa.gov/19880004824.pdf> (accessed 20 December 2016).
180. L. Zhang, J. Vleugels, L. Darchuk, and O. Van der Biest: Magnetic field oriented tetragonal zirconia with anisotropic toughness. *J. Eur. Ceram. Soc.* **31**, 1405 (2011).
181. R. Pavlacka, R. Bermejo, Y. Chang, D.J. Green, and G.L. Messing: Fracture behavior of layered alumina microstructural composites with highly textured layers. *J. Am. Ceram. Soc.* **96**, 1577 (2013).
182. Y. Chang, R. Bermejo, and G.L. Messing: Improved fracture behavior of alumina microstructural composites with highly textured compressive layers. *J. Am. Ceram. Soc.* **97**, 3643 (2014).
183. M-Y. He and J.W. Hutchinson: Crack deflection at an interface between dissimilar elastic materials. *Int. J. Solids Struct.* **25**, 1053 (1989).
184. M. Nakamura, K. Hirao, Y. Yamauchi, and S. Kanzaki: Tribological properties of unidirectionally aligned silicon nitride. *J. Am. Ceram. Soc.* **84**, 2579 (2001).
185. W. Wu, Y. Sakka, and T.S. Suzuki: Microstructure and anisotropic properties of textured ZrB_2 and ZrB_2 - MoSi_2 ceramics prepared by strong magnetic field alignment. *Int. J. Appl. Ceram. Technol.* **11**, 218 (2014).
186. X. Zhu and Y. Sakka: Textured silicon nitride: Processing and anisotropic properties. *Sci. Technol. Adv. Mater.* **9**, 1 (2008).
187. R. Pavlacka and G. Messing: Processing and mechanical response of highly textured Al_2O_3 . *J. Eur. Ceram. Soc.* **30**, 2917 (2010).
188. Z.M. Sun: Progress in research and development on MAX phases: A family of layered ternary compounds. *Int. Mater. Rev.* **56**, 143 (2011).
189. M. Shamma, E.N. Caspi, B. Anasori, B. Clausen, D.W. Brown, S.C. Vogel, V. Presser, S. Amini, O. Yeheskel, and M.W. Barsoum: *In situ* neutron diffraction evidence for fully reversible dislocation motion in highly textured polycrystalline Ti_2AlC samples. *Acta Mater.* **98**, 51 (2015).
190. C. Hu, Y. Sakka, H. Tanaka, T. Nishimura, and S. Grasso: Fabrication of textured Nb_4AlC_3 ceramic by slip casting in a strong magnetic field and spark plasma sintering. *J. Am. Ceram. Soc.* **94**, 410 (2011).
191. C. Hu, Y. Sakka, T. Nishimura, S. Guo, S. Grasso, and H. Tanaka: Physical and mechanical properties of highly textured polycrystalline Nb_4AlC_3 ceramic. *Sci. Technol. Adv. Mater.* **12**, 044603 (2011).
192. C. Hu, Y. Sakka, S. Grasso, T. Nishimura, S. Guo, and H. Tanaka: Shell-like nanolayered Nb_4AlC_3 ceramic with high strength and toughness. *Scr. Mater.* **64**, 765 (2011).

193. C. Hu, Y. Sakka, S. Grasso, T. Suzuki, and H. Tanaka: Tailoring Ti_3SiC_2 ceramic via a strong magnetic field alignment method followed by spark plasma sintering. *J. Am. Ceram. Soc.* **94**, 742 (2011).
194. K. Sato, M. Mishra, H. Hirano, T.S. Suzuki, and Y. Sakka: Fabrication of textured Ti_3SiC_2 ceramic by slip casting in a strong magnetic field and pressureless sintering. *J. Ceram. Soc. Jpn.* **122**, 817 (2014).
195. H.B. Zhang, C.F. Hu, K. Sato, S. Grasso, M. Estili, S.Q. Guo, K. Morita, H. Yoshida, T. Nishimura, T.S. Suzuki, M.W. Barsoum, B.N. Kim, and Y. Sakka: Tailoring Ti_3AlC_2 ceramic with high anisotropic physical and mechanical properties. *J. Eur. Ceram. Soc.* **393**, 35 (2015).
196. M. Mishra, Y. Sakka, C. Hu, T.S. Suzuki, T. Uchikoshi, and L. Besra: Textured Ti_3SiC_2 by EPD in a strong magnetic field. *Key Eng. Mater.* **507**, 15 (2012).
197. Y. Mizuno, K. Sato, M. Mrinalini, T.S. Suzuki, and Y. Sakka: Fabrication of textured Ti_3AlC_2 by spark plasma sintering and their anisotropic mechanical properties. *J. Ceram. Soc. Jpn.* **121**, 366 (2013).
198. T. Lapauw, K. Vanmeensel, K. Lambrinou, and J. Vleugels: A new method to texture dense $\text{M}_{n+1}\text{AX}_n$ ceramics by spark plasma deformation. *Scr. Mater.* **111**, 98 (2016).
199. V.I. Aleshin, I.P. Raevskii, and E.I. Sitalo: Electromechanical properties of a textured ceramic material in the $(1-x)\text{PMN}-x\text{PT}$ system: Simulation based on the effective-medium method. *Phys. Solid State* **50**, 2150 (2008).
200. M. Pham-Thi, H. Hemery, and H. Dammak: X-ray investigation of highly oriented $(1-x)\text{PbMg}_{1/3}\text{Nb}_{2/3}\text{O}_3-(x)\text{PbTiO}_3$ ceramics. *J. Eur. Ceram. Soc.* **25**, 2433 (2005).
201. S.F. Poterala, R.J. Meyer, and G.L. Messing: Low-field dynamic magnetic alignment and templated grain growth of diamagnetic PMN-PT ceramics. *J. Mater. Res.* **28**, 2961 (2013).
202. J.L. Jones, E.B. Slamovich, and K.J. Bowman: Critical evaluation of the Lotgering degree of orientation texture indicator. *J. Mater. Res.* **19**, 3414 (2004).

Supplementary Material

To view supplementary material for this article, please visit <https://doi.org/10.1557/jmr.2017.207>.